Applicability of scaled testing for CAMUI-type hybrid rocket regression modelling

A dissertation presented

by

Tor Viscor

to

The Laboratory of Space Systems

Division of Mechanical and Space Engineering

in partial fulfilment of the requirements

for the degree of

Doctor of Philosophy

Hokkaido University

February 2022

Dissertation Advisor: Harunori Nagata

Tor Viscor

Applicability of scaled testing for CAMUI-type hybrid rocket regression modelling

Abstract

Hybrid rocket engines have several advantages over liquid or solid engines but have traditionally seen limited use due to a low thrust-to-weight ratio. The Cascading Multi-Stage Impinging jet (CAMUI) hybrid rocket engine addresses this by using a series of impinging jets and fountain-like flow paths to improve mixing and increase heat transfer to the solid fuel surface.

This thesis investigates the scaling of the CAMUI regression model over an extensive engine size range for the first time, comparing the model to actual firing data from over 30 hybrid rocket firing tests, ranging from 100 mm-diameter-2.5 kN-class engines to 400 mm-diameter-40 kN commercial class engines.

With the development of a time-stepped regression simulator, identification and quantification of potential regression simulation uncertainties were performed. Burn time, specifically the effect of long start-up transients, was identified as the most critical. Further investigation into the impact of the transient burn time resulted in the proposed method of using burn time equivalent. This method considerably reduced the errors arising from the long start-up transients. Though done for the CAMUI engine, it was shown to be valid for other hybrid rocket engines.

Lastly, with the proposed regression model corrections implemented, the simulator

was used to design the successfully fired 40 kN-class engine. The developed model showed good scalability when evaluating the overall regression simulation model in the order of magnitude scaling range of 100 mm-diameter-2.5 kN-class engines to 400 mm-diameter-40 kN.

This validates the scalability of the CAMUI concepts as well as its regression modeling to large-scale engines, opening the door for commercial implementation of CAMUI for suborbital and orbital-class rockets.

Contents

List of Figures

List of Tables

List of Acronyms

A	cross sectional area
A_p	cross sectional area for port
A_{t_i}	cross sectional area tube inside
A_{tw}	cross sectional area of tube wall
a	function of O/F
a_c	corrected version of a
a_d	function of O/F back-end surface
a_p	function of O/F port
a_u	function of O/F fore-end surface
CAMUI	Cascaded Multi-Stage Impinging Jet
C_{LOX}	specific heat of LOX
C_t	specific heat of feedline tube
c	specific heat
$c1$,$c2$,$c3$,$c4$	empirical constants
$cv0, cv1, cv2, cv3$	empirical constants
$cvd0$, $cvd1$, $cvd2$, $cvd3$	empirical constants back-end surface
$cvp0$, $cvp1$, $cvp2$, $cvp3$	empirical constants Port
$cvu0$, $cvu1$, $cvu2$, $cvu3$	empirical constants fore-end surface
D	diameter

D_p	port diameter
D_{p_i}	initial port diameter
D_{s_i}	initial separator diameter
D_s	separator diameter
d	distance from center to measurement point
$d_{average}$	average distance
F	force of engine thrust
$F_{steadyState}$	force of engine thrust at steady state
f	empirical value
GFRP	glass fibre reinforced plastic
GOX	gas oxygen
G_p	mass flux port
G_{p_p}	propellant mass flux port
G_{p_u}	propellant mass flux upstream
H	separator height after firing
HDPE	high-density polyethylene
H_e	latent heat of evaporation
H_i	initial height
h_v	heat of gasification of the fuel
δh	enthalpy difference of the gas between the fuel surface and flame
I_{sp}	specific impulse
L	length
LOX	liquid oxygen
L_t	length tube

L_{tank}	length tank
m	empirical constant
$\dot{m}$	mass flow rate
$\dot{m}_{LOX}$	LOX flow rate
$\dot{m}_o$	LOX flow rate
m_d	empirical constant back-end surface
m_p	empirical constant port
m_u	empirical constant fore-end surface
N2	nitrogen
n	empirical constant
n_d	empirical constant back-end surface
n_u	empirical constant fore-end surface
O/F	oxidizer to fuel (ratio)
$(O/F)_{ref}$	oxidizer to Fuel (ratio) reference
OMV1, OMV2	oxygen main valve
R	fuel regression
Re	Reynolds number
RMS	root mean square
R_u	fuel regression fore-end surface
r	regression rate
r_d	regression rate back-end surface
r_p	regression rate port
r_u	regression rate fore-end surface
S_t	Stanton number

S_{t_0}	Stanton number without blowing
T	temperature
T_{bl}	oxygen boiling temperature
T_{to}	temperature of tube at time zero
t	time
t_b	Burn time (s)
$t_{b_{eq}}$	equivalent burn time
t_f	flame spreading time
t_t	travel time
t_{t2ph}	time two phase flow
V	volume
V02	oxygen valve
V_{emp}	empty volume of engine
v_e	free stream velocity
v_b	velocity at the flame
X	position
X_{i_p}	initial port O/F ratio
x	each measurement point
ρ	mass density
ρ_{GOX}	GOX density
ρ_{LOX}	LOX density
μ	viscosity

Acknowledgments

The author would like to acknowledge the dedicated support throughout the many years of the project of Mr. Uematsu and his staff, without which this research would never have been possible. Furthermore, a special thanks goes to the supporting academic team led by L. Kamps and H. Nagata and the industrial team led by M. Itoh and K. Yonekura. Last but not least, an enormous thank you to my wife Katia Nagamine Urata not only for her support as a family member but also her professional support in all aspects of writing, coding, publication preparation, and technical feedback, which has been a tremendous help in completing this work.

This work is dedicated to all rocket amateurs.

Chapter 1

Introduction

In recent years, there has been a substantial increase in the development of new rocket systems, with many new companies developing their own launchers. After only a few years, many of these new start-up companies are evaluated in Billion dollars category. With the growth in launcher interest and new rocket development and the resulting massive increase in investments, the hybrid rocket technology has seen a significant increase in development (1). This trend is due to the essentially non-explosive nature of the hybrid propulsion rocket system. Hybrid rockets are inherently safer than their liquid or solid counterparts when the fuel is stored in the solid state and the oxidizer is stored in the liquid form (2), (3), as is the case in this research.

These separate states remove the possibility of uncontrolled mixing, and consequently, an explosion if any engine part ruptures. This robustness against explosion is a strongly desirable trait, especially in the operation of small, low-cost launchers, be they for suborbital or orbital flights. Once the cost of the launcher hardware is low enough, the ground costs become the main expense, with a substantial part of this being

due to risk reduction associated with the explosive nature of conventional solid and liquid bi-propellant rocket engines. Hybrid rockets avoid this cost but have traditionally had too low fuel regression rates and or too small burning surface areas to produce adequate thrust-to-weight ratios for launch rockets or boosters.

The Cascaded Multi-Stage Impinging Jet (CAMUI) engine achieves the high thrust-to-weight ratio needed using the world's most used plastic, polyethylene (4). Through its internal fuel geometry design, the CAMUI engine achieves very high efficiency while keeping the high thrust-to-weight ratio, resulting in a solid contender for a commercial low-cost, low-risk, high-performance rocket engine.

To define the target engine size for first commercialization, the engine size of previous commercially successful sounding rockets was investigated. Figure 1.1 shows the basic engine categories of the most sold sounding rockets over the last years.

Global commercial market**

Skylark series (UK)
Total sold: 400 +
Period: 1960-2020

Blackbrant series (CANADA)
Total sold: 800 +
Period: 1960-2020
Almost always 2 stage configuration
NASA use: 10-20/year

Series (Boosters)	Total sold	Active period	Thrust	Mass
Black Brant (CANADA)	800 +	1960 - now	10-150 kN	100-1200 kg
Skylark (UK)	400 +	1955-2005	50 kN (30 sec)/60 kN (40 sec)	850 kg – 1000 kg
Nike (USA)	500-1000	1953- TBD	217 kN (3 sec)	TBD
Orion (USA)	70	1974 - 2008	7 kN (35 sec)	400 kg
VS-30 (second stage of VSB-30)	50+	1997 - now	100 kN (20 sec)	1400 kg
S31 (first stage of VSB-30)	30+	2004 - now	200 kN (10 sec)	

Figure 1.1: Most sold rockets

With these sizes as input, discussions with launch providers, and balancing cost vs. performance to achieve a low-cost sounding rocket with a reasonable payload capability, an engine performance of 40 kN average thrust over a 20 sec burn time was chosen as a design target. This will result in a 500 kg class sounding rocket capable of lifting a 100 kg payload to an altitude of 120 km.

Previous research over the last two decades on the CAMUI engine type has been limited to smaller engine sizes due to available resources. To move beyond the existing small-scale proof of concept to commercial sounding rocket and launcher-sized engines, understanding the scalability of the CAMUI hybrid rocket regression models is critical (5).

This thesis investigates the scaling of the CAMUI regression model over an extensive engine size range for the first time, comparing the model to actual firing data from over 30 hybrid rocket firing tests, ranging from 100 mm-diameter-2.5 kN-class engines to 400 mm-diameter-40 kN commercial class engines. For comparison, the currently highest thrust commercial hybrid rocket engine worldwide is 80 kN class.

This work is presented in the following chapters:

1. Introduction
2. Regression simulator description;
3. Test setup description;
4. Uncertainty analysis;
5. Uncertainty reduction;

6. Large scale engine;

7. Discussion of Results and Impact on Hybrid Rocket Development;

8. Concluding Remarks.

Chapter 2 describes the baseline mathematical formulas used and touches shortly on their development history. It further goes on to detail how these formulas are incorporated in a new way, namely in a time stepped iterative software regression simulator, allowing for continuous modeling of the regression with the changing geometry of the fuel through the burn as opposed to only modeling the before and after burn time values.

Chapter 3 describes the various test setups used to acquire the data analyzed in this work. HDPE is used as a fuel and LOX as an oxidizer for all the test setups. The systems are pressure fed, and all tests are done with CAMUI style engines. To better be able to control start-up transients, the MSS and O-BASAN test setups have been designed to allow for pre-pressurization of the LOX tank and pre-cooling of the feed-line. This was done by including additional LOX valves in the LOX feed-line.

Chapter 4 describes the uncertainty analysis performed. From this, it was found that the largest simulator error is from the start-up transients, mainly caused by tank pressurization and the movement of LOX through the feed-line. The start-up transients cause an uncertainty in the defined burn time which was shown to have a very large effect on the total regression error. Other uncertainties such as local gasification, Reynolds number grouping, and the limitation of using the diffusion-limited modelling approach only, are also discussed. Lastly, a systematic measurement error in previous work was identified and is described.

Chapter 5 describes the four main steps taken to reduce the model uncertainties. These are:

- Inclusion of local gasification (inclusion of the fuel gasified on a given burn surface to calculate the regression (gasification) of the fuel on that same surface) through the use of the iterative time stepped modeling approach.
- Development of the equivalent burn time to reduce the uncertainty of large transient times. This method attempts to correct the burn time to better model how the burn would be if there were no transients.
- Changes to the test setups to control the start-up transient. These include valves at strategic locations to allow for pre-pressurization of the LOX tank and pre-cooling of the feedline.
- Mathematical Data correction of heritage fuel blocks. As the fuel blocks from some of the tests are no longer available and it is believed there was a systematic measurement error in the measurement of the regression rates, a proposed mathematical data correction is described.

Chapter 6 describes how the work mentioned above was used to develop ever-increasing engine sizes to reach a commercially viable engine size. This 40 kN engine class was successfully fired, and the test results were used to evaluate the overall regression model performance. This showed good scalability of the model with an RMS regression error of 26%.

Chapter 7 then summarizes the above results and discusses how these potentially can impact the development of hybrid rockets both within the CAMUI technology and

outside. Overall many of the findings in the uncertainty analysis are just as valid for any hybrid rocket research though the actual uncertainty values will differ depending on the design. Likewise, the corrections suggested can be used directly or adapted depending the engine design for both CAMUI style and non CAMUI style engines. For the further development of the CAMUI engine itself, the model proved to be more than adequate to allow rapid engine development.

Lastly, Chapter 8 concludes this work in the context of the starting goal of developing a commercial size CAMUI engine. This work satisfies the primary target, which was to develop a scaled regression model that would allow us to rapidly develop a large-sized engine, in this case, the 40 kN class. It is worth noting that programmatic risk management regarding other aspects of engine combustion, namely potential ignition instabilities, was the main reason for not developing faster than was done. The model described in this work made it possible both to technically develop the end goal 40 kN engine and convince investors and research partners to finance and support the development. The firing of this 40 kN engine finalized the proof-of-concept development for a viable sounding rocket engine.

Further development to mass optimize the engine and push the possible burn time as far as possible is currently underway under the company MSW, which was started in 2020 to develop and commercialize this engine and a future larger engine.

Chapter 2

Regression model and design method

2.1 Main concept of CAMUI geometry

The principle of the CAMUI fuel geometry is shown in Figure 2.1. This geometry causes the hot combustion gas to impinge multiple times on the fuel surfaces when exiting each port, thereby significantly increasing convective heat transfer to the fuel and, consequently, the fuel regression rate and overall engine thrust-to-weight ratio.

2.2 Mathematical regression model

For the regression modelling the following definition of the fuel geometry is used as shown in Figure 2.2. The core baseline of the mathematical regression model is Marxman's diffusion-limited model (6). Namely, Equation 2.1.

$$\textbf{Tubular port fuel: } r_p = a_p G_p^{m_p} \tag{2.1}$$

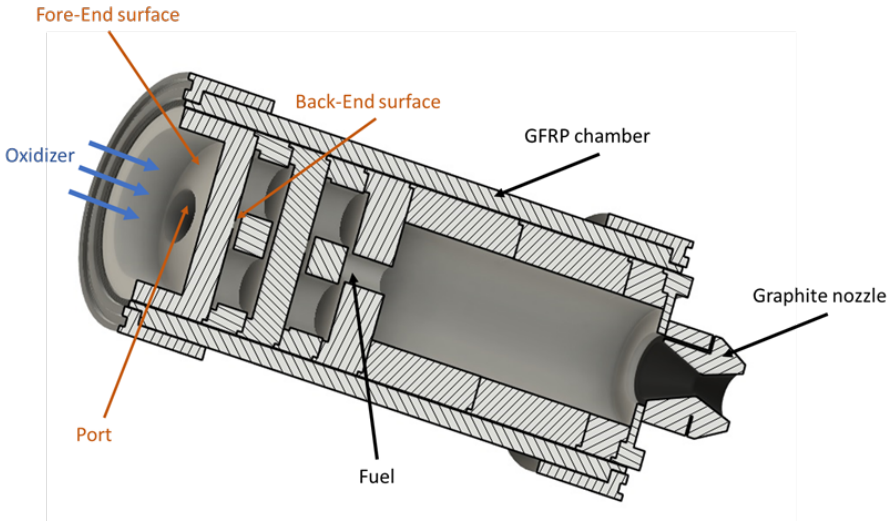

Figure 2.1: CAMUI hybrid rocket design principle.

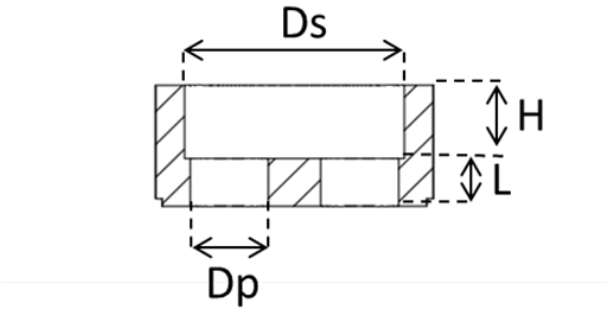

Figure 2.2: Fuel geometry definition.

This though is for a typical tubular (port) geometry of the fuel and though representative for the port regression of the CAMUI fuel, it does not cover the impinging gas effect experienced on the two end faces of the CAMUI fuel. To take this into account, (7) developed the Equations 2.2-2.6.

$$\textbf{For upstream end face: } r_u = a_u G_p^{m_u} \left(\frac{H}{D_p}\right)^{n_u} \tag{2.2}$$

$$\textbf{For downstream end face: } r_d = a_d G_p^{m_d} * (H)^{n_d} \tag{2.3}$$

$$\textbf{With } a \textbf{ theoretical given by: } a = \frac{c}{\rho}\frac{(\mu)^{1-m}}{D^{1-m}}\frac{S_t}{S_{t_0}}\frac{v_e}{v_b}\frac{\delta h}{h_v} \tag{2.4}$$

$$\textbf{With } a \textbf{ empirically defined by: } a = cv0 + cv1 * exp[-(\frac{(ln(\frac{O/F}{cv2}))}{cv3})^2] \tag{2.5}$$

$$\textbf{With } G_p \textbf{ : } G_p = (\frac{m_p}{2A_p}) \tag{2.6}$$

As is discussed in (8), the theoretical formulation for a is based on the assumption that the regression rate of the fuel surface is proportional to the heat flux to the fuel surface. Further it is assumed that the heat transfer arises from turbulent convection, that the chemical reaction rate is infinite compared to the species transfer rate and lastly that the flame has zero thickness. These conditions allow us to use the theoretical expression shown in Equation 2.7 upon which Equations 2.2-2.6 are based. This also includes Equation 2.4 which is proportional to $\frac{1}{D^{1-m}}$. The value a in this as well as previous research is determined as an empirical function of O/F and does not take changing D values into account. To make the derived values of a valid over a range of scaled values of D, in (8) and (5), a scaling term was added to Equations 2.1-2.3.

Lastly in (8), it was identified that specifically for the downstream end face, the changing of the height H between the end faces also had an important role in scaling of the engines. To take this into account, an additional scaling factor was included to

Equation 2.3. The resulting regression equations including the scaling terms are shown Equations 2.8-2.10:

$$\textbf{Tubular fuel regression: } r = \frac{c}{\rho}\frac{(\mu)^{1-m}}{D^{1-m}}\frac{S_t}{S_{t_0}}\frac{v_e}{v_b}\frac{\delta h}{h_v}G_p^p \tag{2.7}$$

$$\textbf{For upstream end face: } r_u = a_u G_p^{m_u}(\frac{H}{D_p})^{n_u} * (\frac{D_p}{D_{pi}})^{m_u-1} \tag{2.8}$$

$$\textbf{For port wall: } r_p = a_p G_p^{mp} * (\frac{D_p}{D_{pi}})^{m_u-1} \tag{2.9}$$

$$\textbf{For downstream end face: } r_d = aG_p^(m_d) * (\frac{H}{H_i})^{n_d} * (\frac{D_p}{D_{pi}})^{(m_d-1)} \tag{2.10}$$

The starting point for this research is therefore based on the above resulting in the mathematical model of the fuel block regression being as shown in Equations 2.11-2.16.

$$\textbf{For upstream end face: } r_u = aG_p^{m_u}(\frac{H}{D_p})^{n_u} * (\frac{D_p}{D_{pi}})^{(m_u-1)} \tag{2.11}$$

$$\textbf{For port wall: } r_p = aG_p^{m_p} * (\frac{D_p}{D_{pi}})^{(m_p-1)} \tag{2.12}$$

$$\textbf{For downstream end face: } r_d = aG_p^(m_d) * (\frac{H}{H_i})^{(n_d)} * (\frac{D_p}{D_{pi}})^{(m_d-1)} * (\frac{D_p}{D_{pi}})^{(m_p-1)} \tag{2.13}$$

$$\textbf{With } a \textbf{ theoretical given by: } a = \frac{c}{\rho}\frac{\mu^{1-m}}{D^{1-m}}\frac{S_t}{S_{t_0}}\frac{v_e}{v_b}\frac{\delta h}{h_v} \tag{2.14}$$

$$\textbf{With } a \textbf{ theoretical given by: } a = cv0 + cv1 * exp[-(\frac{(ln(\frac{O/F}{cv2}))}{cv3})^2] \tag{2.15}$$

$$\textbf{With } G_p \textbf{ : } G_p = (\frac{m_p}{2A_p}) \tag{2.16}$$

2.3 Software Implementation of Regression Model

Previous research has been based on simulating the regression of an engine as an averaged constant regression rate through the burn time. As the dimensions can change considerably through the burn time this can have an effect on the regression simulated. Previous research often quotes the ratio between the port diameter and the length of the port. With port diameter typically doubling through burn time and port length going to zero for a fully burned fuel block this ratio changes drastically. To counter this an iterative time stepped regression simulator was developed allowing for continuously updating of the fuel dimensions and therefore regression rates during the entire burn time.

As shown in Figure 2.3, the CAMUI simulator is split into three parts. The database which is the repository of previously fired engines, the constants analyser that extracts the empirical constants needed, and lastly, the regression simulator, which by using these constants, simulates the continuous regression of the burn surfaces throughout the burn time.

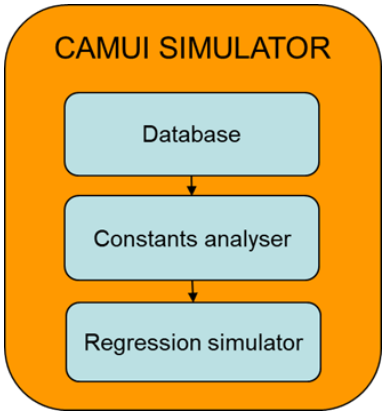

Figure 2.3: CAMUI simulator overview.

2.3.1 Database

The database here contains the gathered data from the previous firings of respectively the 2.5 kN class RIE test series of engines and the 10 kN class TTY test series of engines. The following data is contained for each engine firing:

For each fuel block:

- Separator diameter before firing (D_{s_i})
- Separator diameter after firing (D_s)
- Port diameter before firing (D_{p_i})
- Port diameter after firing (D_p)
- Separator height before firing (H_i)
  - Distance from upstream end face to downstream end face of the fuel block above (or injector for the first fuel block)
- Separator height after firing (H)

– Averaged distance from upstream end face to downstream end face of the fuel block above (or injector for the first fuel block)

For each engine:

- LOX flow measured throughout burn time
- Chamber pressure measured throughout burn time
- Thrust measured throughout burn time
- Burn time

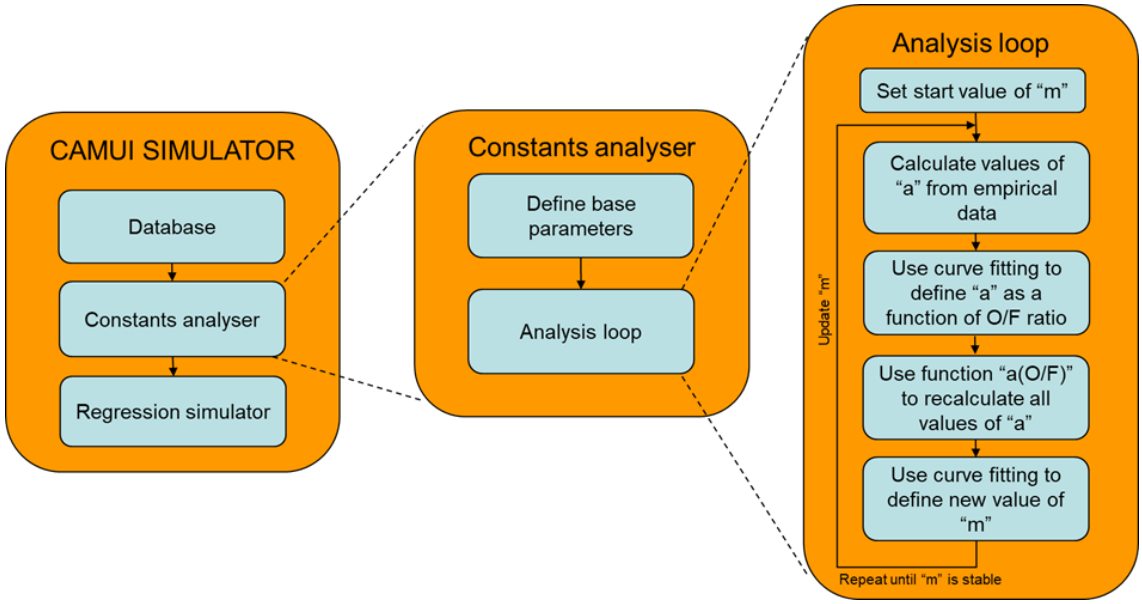

Figure 2.4: Constants analyser principle (port example).

2.3.2 Constants Analyser

Based on the data from a chosen test series in the database, the constants analyser extracts the m values and $a(O/F)$ functions for each of the burn surfaces, upstream end

face, port, and downstream end face. Figure 2.4 shows the overall flow of extracting the m-values and the a functions which follows the methodology described in (8).

Port Calculation Method

To extract the values for a and m, for the port, the following method based on (8) was used. First, an assumed value for the coefficient m is chosen; in this case $m = 0.5$ was taken as a starting point. After the first iteration, the resulting m from the calculation updates the new assumed m. Based on this, the coefficient a_c is calculated according to Equation 2.17.

$$a_c = \frac{r_p}{G_p^m * (\frac{D_p}{D_{pi}})(m-1)} \tag{2.17}$$

With a_c, the corrected version of a, taking into account the scaling caused by the increase of the port diameter during the burn. The component $(\frac{D_p}{D_{pi}})^{(m_d-1)}$ represents this scaling, with D_p being the averaged port diameter through the burn and D_{pi} being the initial port diameter.

a_c is then plotted vs O/F (which is measured by block fuel regression, oxidizer mass flow and burn time). This plot is then fitted with the Eq 19 to find the best fitted values for $cv0$, $cv1$, $cv2$ and $cv3$:

$$a_c = cv0 + cv1 * exp[-(\frac{ln((O/F)/cv2)}{cv3})^2] \tag{2.18}$$

To the best of the author's knowledge, Equation 2.18 was chosen for its reasonable fitting to the data alone and not for any analytical or theoretical reason. For the curve

fitting, the Matlab *fit* function was used. $a_c(O/F)$ is then recalculated using Equation 2.18 with the found $cv0$, $cv1$, $cv2$ and $cv3$.

Likewise, $a_c((O/F)_{ref})$ is then recalculated using Equation 2.19 with the $(O/F)_{ref}$ value, $(O/F)_{ref} = 5$ in this case, and the same found values $cv0$, $cv1$, $cv2$ and $cv3$.

$$a_c(O/F)_{ref} = cv0 + cv1 * exp[-(\frac{ln((O/F)_{ref}/cv2)}{cv3})^2] \tag{2.19}$$

$$r_p(O/F)_{ref} = r_p * ((a_c(O/F)_{ref})/(a_c(O/F))) \tag{2.20}$$

If this value of m differs from the assumed m used in Equation 2.17, this becomes the new assumed m and the calculation is restarted from Eq 18 in a new iteration of the calculations. This is done until m from this last step does not differ from the assumed m last used in Equation 2.17. At this point the found m is taken to be the correct m value for the engine port regression calculations. The full iterative calculation flow is shown in Figure 2.5.

Upstream End Face Calculation Method

The upstream calculation method is done in the same way but using Equation 2.22 instead of Equation 2.17 and Equation 2.23 instead of Equation 2.21: From previous research on the given engines (RIE and TTY), the value of n is set for the upstream end face at $n = -0.26$.

$$\frac{r_p(O/F)_{ref}}{(\frac{D_p}{D_{p_i}})(m-1)} = a_c((O/F)_{ref} * G_p^m \tag{2.21}$$

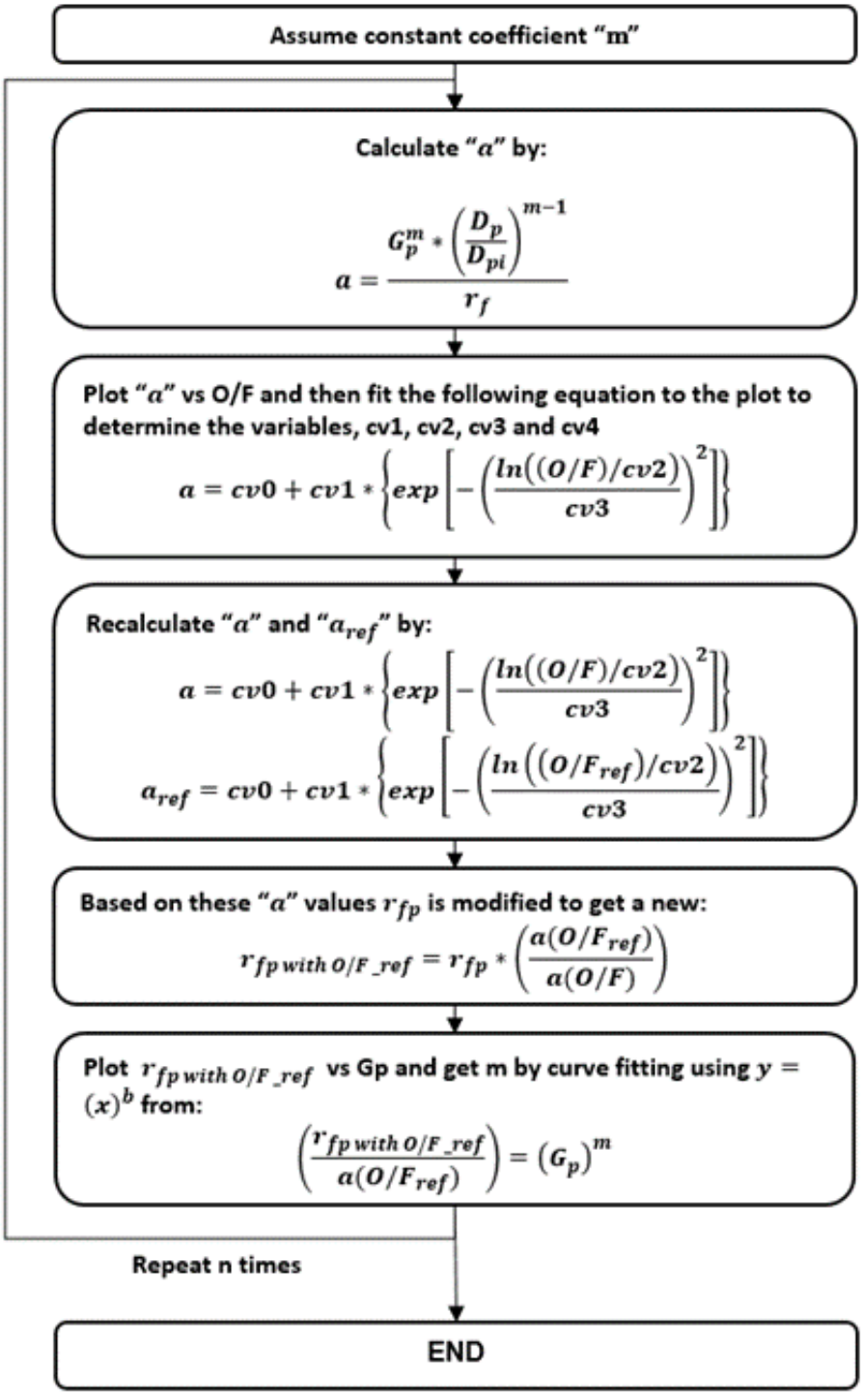

Figure 2.5: Flow for calculating a and m for port regression

$$a_c = \frac{r_u}{(G_p^m)(\frac{H}{D_p})^n(\frac{D_p}{D_{p_i}})^(m-1)} \tag{2.22}$$

Downstream End Face Calculation Method

The upstream calculation method is done in the same way but using Equation 2.24 instead of Equation 2.17 and Equation 2.25 instead of Equation 2.21.

From previous research on the given engines (RIE and TTY), the value of n is set for the upstream end face at $n = -1$.

$$\frac{r_u(O/F_{ref})}{(\frac{H}{D_p})^n(\frac{D_p}{D_{p_i}})^(m-1)} = a_c(O/F)_{ref}G_p^m \tag{2.23}$$

$$a_c = \frac{r_d}{(G_p^m * (H/H_i)^n * (D_p/D_{p_i})^(m-1))} \tag{2.24}$$

$$\frac{r_u(O/F)_{ref}}{(\frac{H}{H_i})^n(\frac{D_p}{D_{p_i}})^(m-1)} = a_c(O/F)_{ref}G_p^m \tag{2.25}$$

The following 17 constants are then the output from the Constants Analyzer:

- m_u
- m_p
- m_d
- $cvu0$, $cvu1$, $cvu2$ and $cvu3$ for Upstream
- $cvp0$, $cvp1$, $cvp2$ and $cvp3$ for Port

- $cvd0$, $cvd1$, $cvd2$ and $cvd3$ for Downstream
- n_u
- n_d

2.3.3 Regression Simulator

Based on the constants derived from the constants analyser and using the regression equations (2.11-2.13 and 2.15), the regression simulation flow is as shown in Figure 2.6. An example of one iteration loop for the regression calculation is depicted in Figure 2.7.

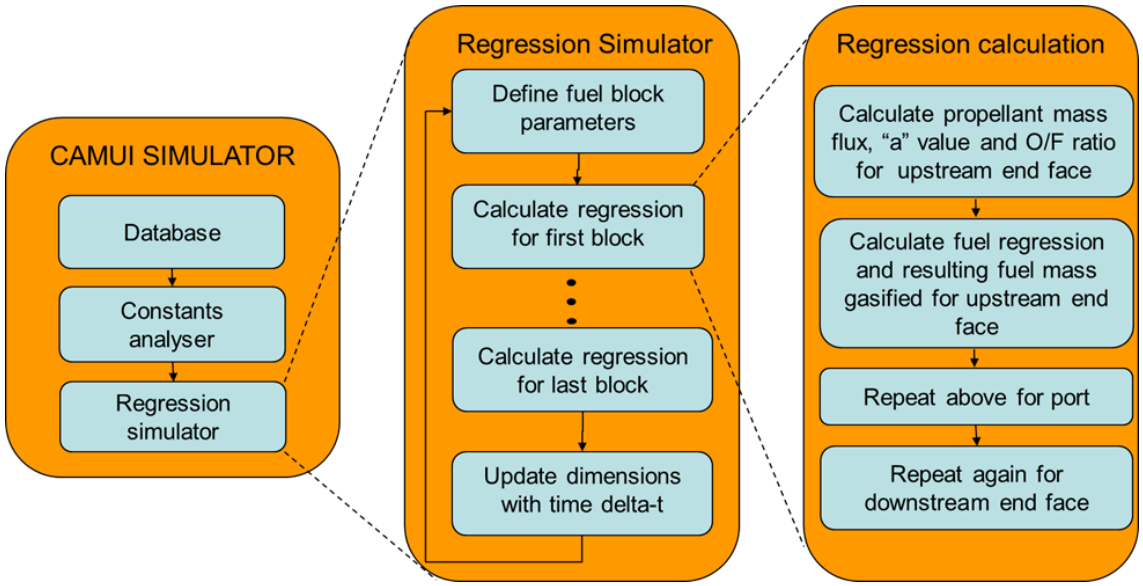

Figure 2.6: Regression simulator flow.

As can be seen, the loop starts with calculating the mass flux. For all surfaces the mass flux is calculated from the total propellant mass flow divided by the upstream port area. This is in line with previous research (8) and (7) which specifically use the port mass flux to calculate the end face regression. Each of the output variables depicted in

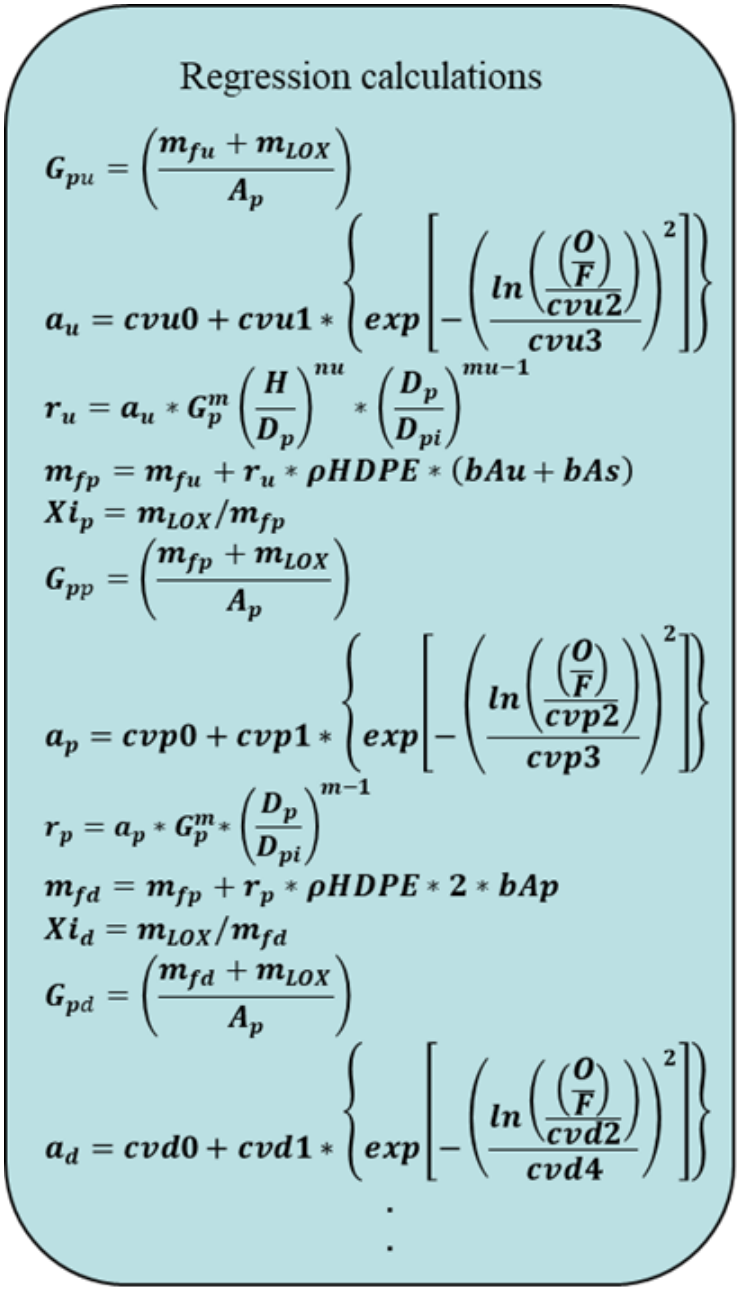

Figure 2.7: Regression calculation loop.

Figure 2.7 are explained as follows:

- G_{p_u}: The propellant mass flux for the upstream end face is calculated from Equation 2.16. The mass flow used is the LOX flow, which is known, plus the

accumulated regressed mass from all upstream burn surfaces. For the first fuel block up stream end face the propellant mass flow is the LOX mass flow alone.

- a_u: The value of a for the given upstream end face is then calculated from Equation 2.15 based on the O/F ratio and the upstream constants $cvu0 - cvu3$. Note that to avoid an infinite O/F ratio for the first block upstream end face a maximum O/F ratio of 150 is set for the first time loop, and for subsequent time loops the O/F ratio is estimated based on the regression calculated on that surface from the previous time loop.

- r_u: The regression rate for the upstream end face is then calculated from Equation 2.11 based on the previously found au value. Here it is important to note that D_{pi} is the design port dimension of the analysed fuel block series used to derive the m values and the a functions. It is not the initial port diameter of the simulated fuel block.

- m_p: The fuel mass flow that enters the port is then calculated as the fuel mass flow entering the previous burn surface (m_{fu}) plus the calculated regression rate r_u times the burn upstream surface area times the fuel mass density.

- X_{i_p}: The O/F ratio (X_i) is calculated from the above m_{fp} and the LOX flow rate

- G_{pp}: This mass flow is then together with the LOX flow used as the propellant mass flow to calculate the port propellant mass flux.

- a_p: The value a_p is then again calculated from Equation 2.15 based on the port O/F ratio (X_{i_p}), and the port constants $cvp0 - cvp3$.

- r_p: The regression rate for the port is then calculated from Equation 2.12 based on the previously found a_p value.

- m_d: The fuel mass flow that enters the downstream end face is then calculated as the fuel mass flow entering the previous burn surface (m_p) plus the calculated regression rate r_p times the upstream surface burn area times the fuel mass density.

- X_{i_d}: The O/F ratio (X_i) is calculated from the above m_{fd} and the LOX flow rate

- a_d: The value a_d is then again calculated from Equation 2.15 based on the port O/F ratio (X_{i_p}), and the port constants $cvd0 - cvd3$.

- r_d: The regression rate for the downstream end face is then calculated from Equation 2.13 based on the previously found a_d value.

- m_u: The fuel mass flow that enters the upstream end face of the next fuel block is then calculated as the fuel mass flow entering the the previous burn surface (m_d) plus the calculated regression rate r_d times the burn upstream surface area times the fuel mass density. This then follows to the G_{p_u} calculation for the next fuel block and the loop repeats itself until all fuel blocks have been calculated.

Based on the simulated time resolution (0.01 sec in this work) and the calculated r_u, r_p, and r_d values that were calculated for each individual fuel block, the dimensions for each of the fuel blocks is updated to represent the material that has been burned away in the last time step.

All calculations are then repeated until the total simulated time is the same as the given total burn time.

Chapter 3

Test Setup

The following engines were used in this work:

Table 3.1:: Engines used in this research.

Engine name	**RIE**	**TTY**	**MSS**	**O-BASAN**
Fuel outer diameter (mm)	100	230	200	400
Nominal thrust level (kN)	2.5	10	2-4	40
Initial fuel mass (kg)	2	25	7-8	125
Propellant flux (kg/s/m2)	200-570	290-740	50-800	230-420
Nr. of fuel blocks/engine	10	10	7-9	16
Burn times (s)	2-5	5-10	5-25	7

The RIE and TTY engines are heritage engines from previous research
The MSS series was a new engine designed under this research with comparatively larger ports to minimize the shift of the O/F ratio throughout the burn. A small thrust,

low mass flux version, and a high thrust, high mass flux version were designed. The O-BASAN series was a new engine designed under this research with comparatively small ports to maximize fill factor within the commercial engine target performance.

3.1 RIE/TTY

All RIE and TTY series tests were performed with similar test setups like the ones shown in Figure 3.1 and Figure 3.2. In preparation the LOX tank and helium tanks are filled. At this point the valve between them (R01) is closed. A chemical igniter, based on a heating wire encased in an epoxy/gunpowder mixture is then lit inside the engine, after which the main valve R01 is opened. This allows Helium to pressurize the LOX tank, thereby forcing the LOX to flow into the engine and combustion to occur. After the set burn time, R01 is closed, cutting off the LOX flow to the engine and ending the burn. The LOX flow is measured using the pressure sensors upstream (P02) and downstream (P03) of the orifice previously characterized.

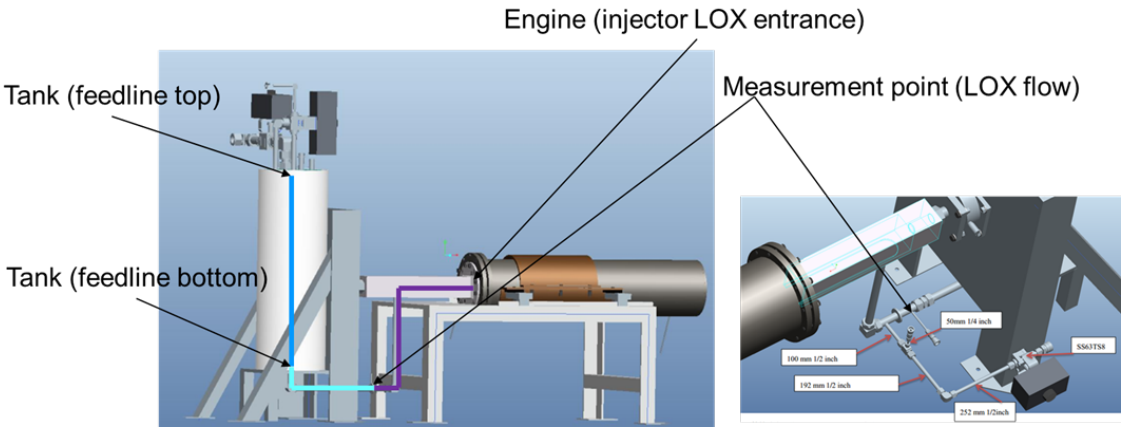

Figure 3.1: TTY test setup.

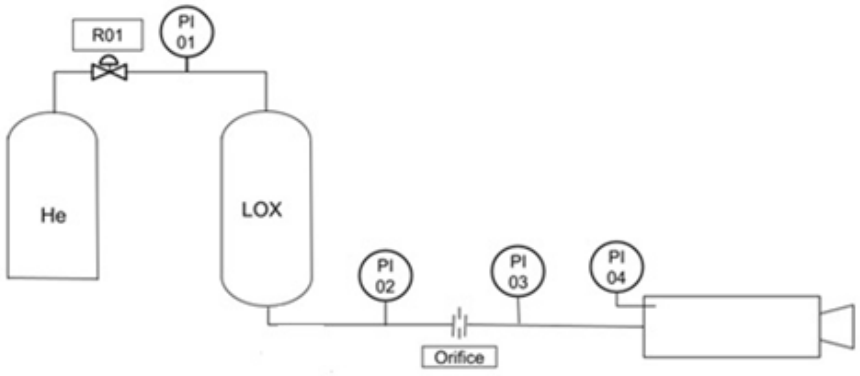

Figure 3.2: TTY/RIE schematic.

3.2 MSS

For the MSS series, the same test setup as used for the TTY series was used. It was modified to add the additional valves V01 and V02. These valves allowed for the pre-pressurization of the tank reducing the start-up transient. This test setup is shown below in Figure 3.3.

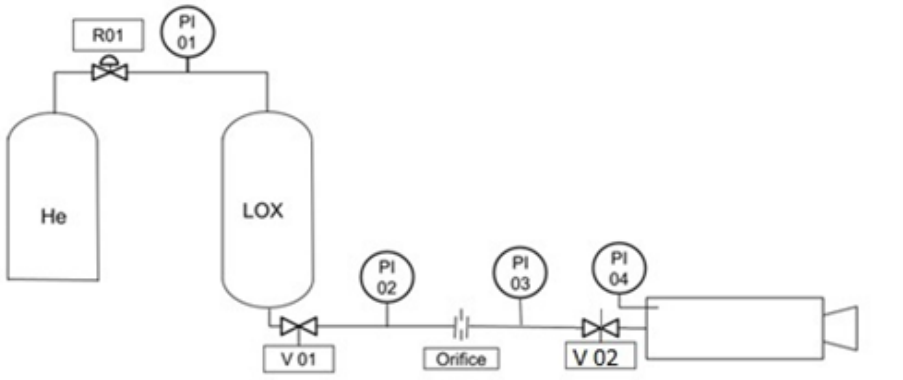

Figure 3.3: MSS series test setup.

A photograph of the actual test setup is shown in Figure 3.4.

As can be seen, to shorten the transient time, the valve V02 was positioned as close

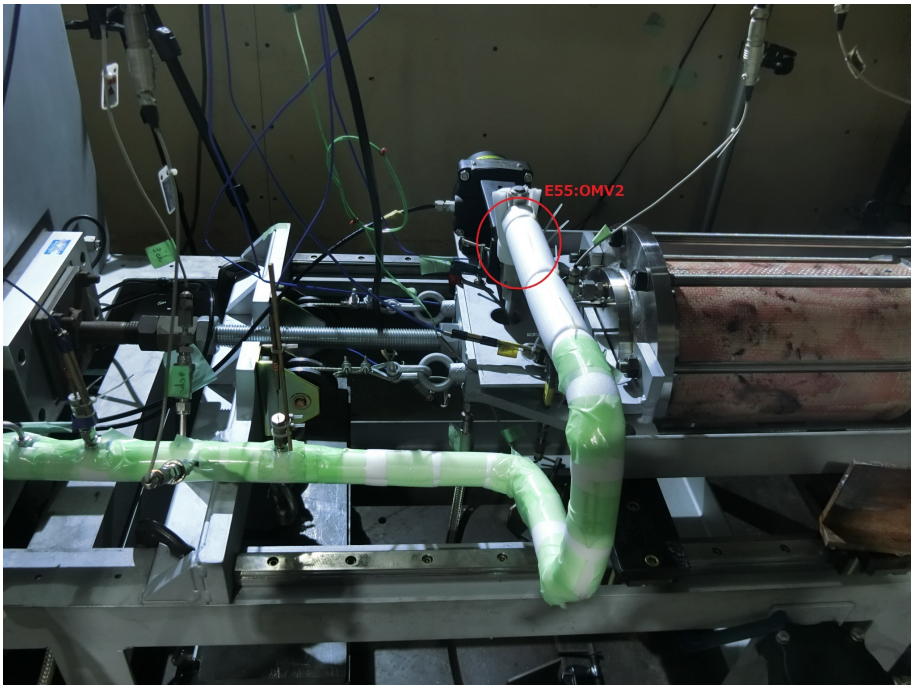

Figure 3.4: MSS test setup photo.

as possible to the engine injector.

A view of the test setup under firing is shown in Figure 3.5. Note the protective steel container around the test setup and the sound baffler (tubular shape in right of picture).

Figure 3.5: Test setup: MSS 04 under firing.

3.3 O-BASAN

For the O-BASAN, the existing test setups were not large enough, neither in physical size nor in thrust capability. As a result, a new test stand was developed. The principle of the feed system followed the MSS test series, though without the V02. As this was a very large combustion surface area and volume increase compared to previous tests, the very short start-up transient given by V02 was deemed risky for ignition instabilities and therefore not used.

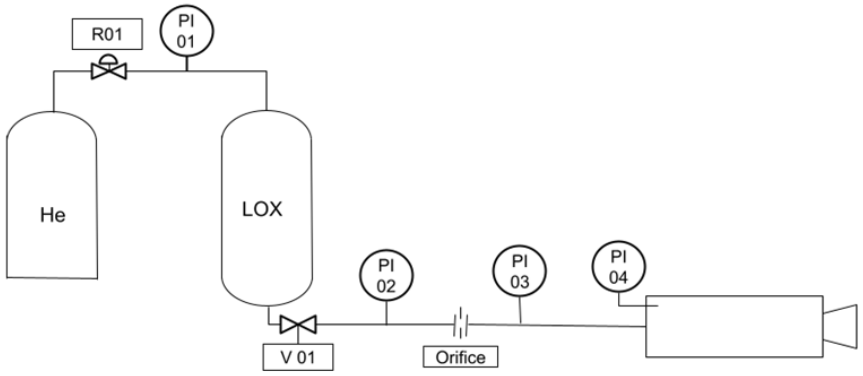

Figure 3.6: BASAN /O-BASAN test setup.

It is important to note that in the discussion of scaling, all previous test setup, fuels and engines could be handled by a single person. As Figure 3.7 shows, this test setup was a completely different scale of size and accompanying effort.

Figure 3.7: O-BASAN engine casing being lowered onto test stand.

Chapter 4

Uncertainty analysis

The overall regression simulator described in the previous section was based completely on the regression equations from previous research. The overall simulation errors can be seen when using this simulator to run simulations of previously performed engine tests and compare the results with the measured regressions. These are shown below in Fig. 4.1.

To identify which areas of research would have the largest effect on the errors seen in Fig. 4.1, an analysis of potential uncertainties that are linked to the used regression model was performed as published in (9). The identified potential uncertainty factors analyzed are:

- LOX travel time
- 2-phase flow
- Tank pressurization time
- Time of ignition flame spreading

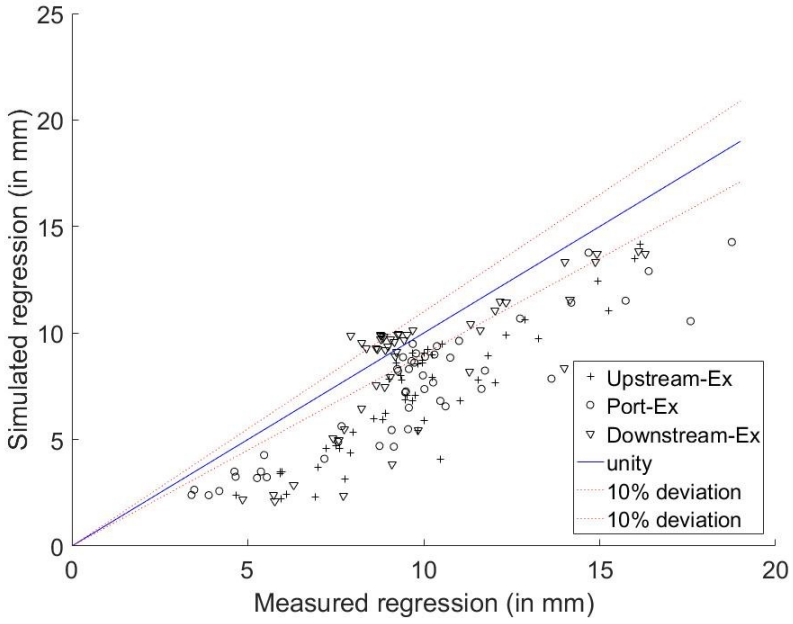

Figure 4.1: CAMUI regression simulator performance (TTY-engines 1-6).

- Local burn surface gasification
- *Re* values
- Model assumptions

The engine series used for this analysis were the TTY-series and the RIE-series. Unless specifically mentioned, the work in this analysis section is done based on the TTY-series data. Specifically, engine TTY 04 is used in some examples. The core information of this engine testing is shown in Table 4.1.

Table 4.1:: TTY04.

Engine	Average Thrust (kN)	Burn time (s)	Fuel blocks	Fuel	Oxidizer
TTY04	6	5.3	10	HDPE	LOX

4.1 Identified uncertainties

The objective of this section is to carefully review the assumptions and other factors that lead to errors in the standard regression model that often get overlooked. The details will be specific to the test setup used in this study. Still, the concept of the uncertainty analysis and many of the physical phenomena identified that lead to the errors seen in the regression simulation are believed to be shared among hybrid rocket researchers.

4.1.1 LOX travel time

As mentioned in Section 3, the oxidizer flow rate is measured by measuring the pressure drop over a previously characterized orifice. This method works under the assumption that the material flowing through it is in a known state, i.e., purely gaseous state or purely liquid state. In our case, we assume a strictly liquid form for the LOX mass flow rate calculations.

The method of LOX feeding is by pressurizing the LOX tank with Helium under a regulated pressure and with the feedline empty prior to tank pressurization. The time delay for the LOX to travel from the tank (feedline top) to the engine (injector) in Figure 3.1 is calculated as shown in Equation (4.1):

$$t_t = \frac{A_{t_i} \cdot (L_t + L_{tank}) \cdot \rho_{LOX}}{\dot{m}_o}. \tag{4.1}$$

As t_t is not directly used in the regression simulator, its effect on burn time (t_b) and LOX flow rate ($\dot{m}_o$) error are estimated instead.

4.1.2 2-phase flow

Under normal test conditions, the feed line is close to ambient temperature resulting in evaporation or partial evaporation of the LOX as it flows through the feed-line. This is important for the LOX flow measurement as the measurement is only valid for oxygen in a fully liquid state. During the start-up the oxygen will be in a partial evaporated state (2 phase state) until the feed-line has been sufficiently cooled for the evaporation to become negligible. The theoretical time it takes for this was calculated in Ref. (10) but not taking into account the latent heat of evaporation of the LOX. With this included, the two-phase time becomes as shown in Eq. (4.2).

$$t_{t2ph} = \frac{C_t \cdot (T_{to} - T_b l) \cdot \rho_t \cdot A_{tw} \cdot L_t}{C_{LOX} \cdot (T_b l - 90) \cdot \dot{m}_o + H_e \cdot \dot{m}_o \cdot f}. \tag{4.2}$$

When the pressure measurement of the orifice downstream pressure is seen to rise, it is assumed that the LOX has returned to a mostly fully liquid state. f is then the empirical value of the fraction of the LOX that is vaporized. It is found by iterating the calculated values to this pressure rise point in the pressure graphs of the engine firing. As t_{t2ph} is not directly used in the regression simulator, its effect on burn time (t_b) and LOX flow rate ($\dot{m}_o$) error are estimated.

4.1.3 Tank pressurization time

Under normal test conditions, the LOX tank pressurizes relatively slowly. The time it takes from the beginning of pressurization to the tank reach steady state is defined as the tank pressurization time. It is evaluated manually from the pressure graphs of the given test firing.

4.1.4 Time of ignition flame spreading

The ignition of the engine is done through an epoxy/gunpowder-covered nichrome wire which is placed on the upstream end face of the first fuel block. It is assumed that at firing, the burning gasses from this local area then spread through the rest of the engine igniting fuel as it flows downstream and around the entire upstream surface of the first fuel block. Based on this, the flame spreading time is calculated by Eq. (4.3):

$$t_f = \frac{V_{emp} \cdot \rho_{GOX}}{\dot{m}_o}. \tag{4.3}$$

As t_f is not directly used in the regression simulator, its effect on burn time (t_b) error is estimated.

4.1.5 Local burn surface gasification

In the regression simulator, the upstream oxygen and gasified fuel are used to calculate the O/F ratio and the mass flux. An example of these calculations for the upstream end face are shown in Equations (4.4) and (4.5):

$$O/F_u = \frac{\dot{m}_{LOX}}{\dot{m}_p}. \tag{4.4}$$

$$G_{pu} = \frac{m_p + \dot{m}_{LOX}}{A_p}. \tag{4.5}$$

The idea of including the local fuel gasification is illustrated for the upstream end face example in Fig. 4.2.

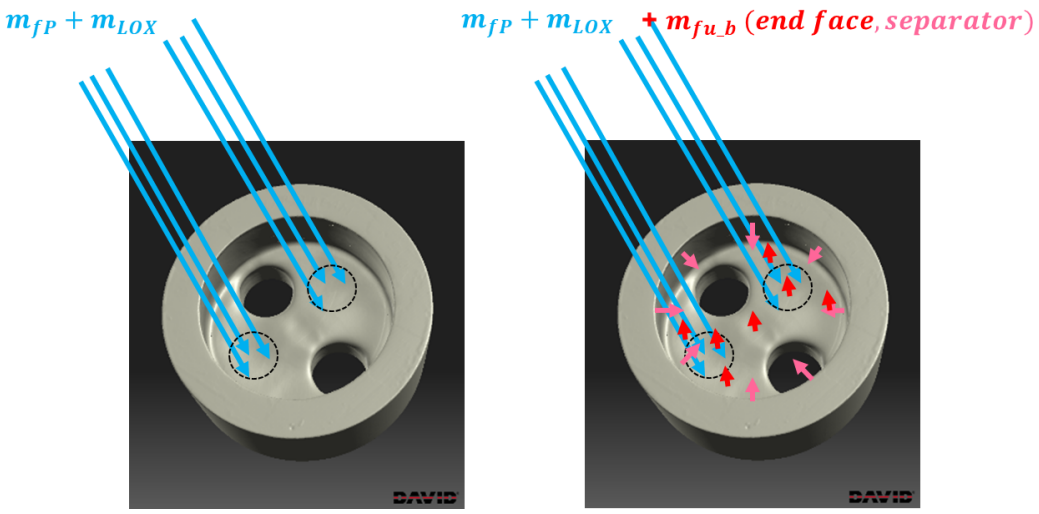

Figure 4.2: Without (left) and with (right) local fuel gasification.

This locally gasified fuel was not previously included in the regression model for the calculations of O/F ratio and propellant mass flux G_p. Including this local fuel gasification, Eqs. (4.4) and (4.5) become Equations (4.6) and (4.7):

$$O/F_u = \frac{\dot{m}_{LOX}}{m_p + m_u}. \tag{4.6}$$

$$G_{p_u} = \frac{m_p + m_u + \dot{m}_{LOX}}{A_p}. \tag{4.7}$$

4.1.6 *Re* values

In the equations of the current regression model (Equations (2.11) to (2.13)) it is assumed that the empirically derived m exponents are constant. Ref. (11) though shows that the m exponent can be dependent on Re with m values ranging from 0.5 to 0.8 for Re values between 10^4 and 10^5. Table 4.2 shows the Re value ranges of the TTY engine series .

Table 4.2:: Reynolds number range TTY.

Engine (TTY)	01	02	03	04	05	06
Max Re [10^5]	5	10	4	6	10	9
Min Re [10^5]	2	3	1	2	2	2

And Table 4.3 Shows the equivalent values for the Re for the RIE- series.

Table 4.3:: Reynolds number range RIE.

Engine (RIE)	01	02	03	04	05	06	07
Max Re [10^4]	20	20	30	20	20	10	10
Min Re [10^4]	7	6	1	9	8	6	5

The potential uncertainty is then estimated using the found Re values to estimate their resulting m values from (11). This change in m values forms the basis of the uncertainty evaluation.

4.1.7 Model assumptions

The measured vs. simulated regression for the different burn surfaces for the TTY04 test firing is shown in Figure 4.3 This gives an idea of the spread of error of the different

burning surfaces and fuel blocks.

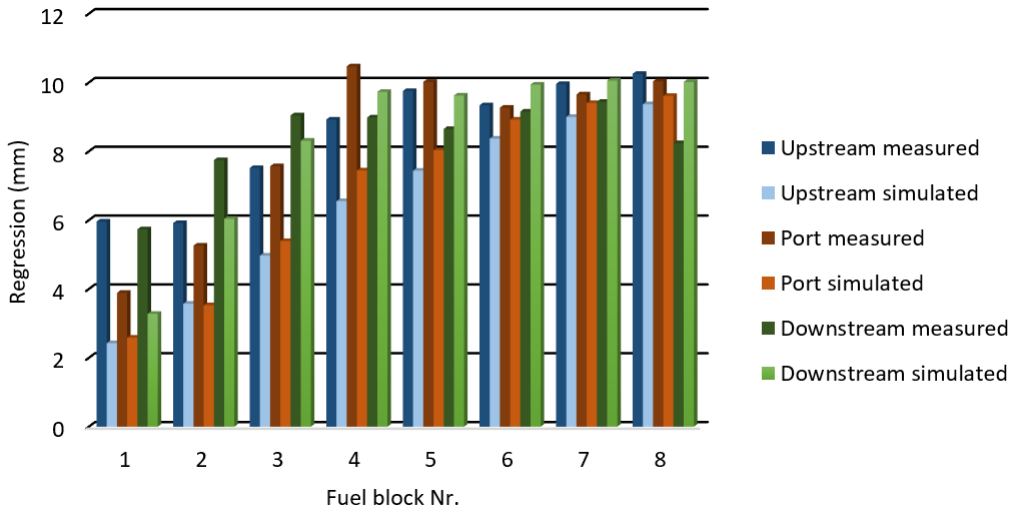

Figure 4.3: Regression simulator error distribution (TTY04).

In Fig. 4.3 the fuel block closest to the injector is block one, and the CAMUI block closest to the nozzle is block 8. The other engines in the TTY series show a similar error spread. The most significant error is clearly on the first fuel block. This error will cause an error in the following mass flux term G_p for the downstream burn surfaces, causing errors on these burn surfaces. To evaluate this, the regression simulation is run with the regression of the upstream end face of block one forced to fit the measured regression.

4.2 Regression model sensitivity

To investigate the sensitivity of the regression simulator, regression simulations are run with errors added to specific values. This is done for each identified core value linked to the evaluated uncertainties with the actual error size ranging from ±1% to ±30% as relevant. The results are then compared to evaluate the severity of the identified error sources.

4.3 Results

4.3.1 Potential simulator input errors

LOX travel time

Using Eq. (4.1) to calculate the LOX travel time in the case of TTY04 gives Eq. (4.8):

$$t_t = \frac{3.8 \cdot 10^{-4} \cdot (1.5 + 0.8) \cdot 1142}{1} = 1s. \tag{4.8}$$

Looking at the terms separately, we get the following:

Tank to measurement point = 0.6 s.

Measurement point to engine = 0.4 s.

The typical test burn times have been between 2 s and 10 s. This gives a potential LOX flow error of $\approx 5 - 25\%$. In the same way, it gives a potential error in the burn time of $\approx 10 - 50\%$.

2-phase flow

Fig. 4.4 shows the LOX flow pressure measurements of the TTY04 firing.

Taking into account the 0.6 s LOX flow travel time, from the tank to the pressure measurement point, this results in a t_{t2ph} of 0.2 s for the first section of the feedline (light blue in Fig. 3.1) and a resulting f value of 0.3. For the full feedline (from the tank to the injector) (light blue and purple in Fig. 3.1) the 2-phase time for the TTY04 firing is

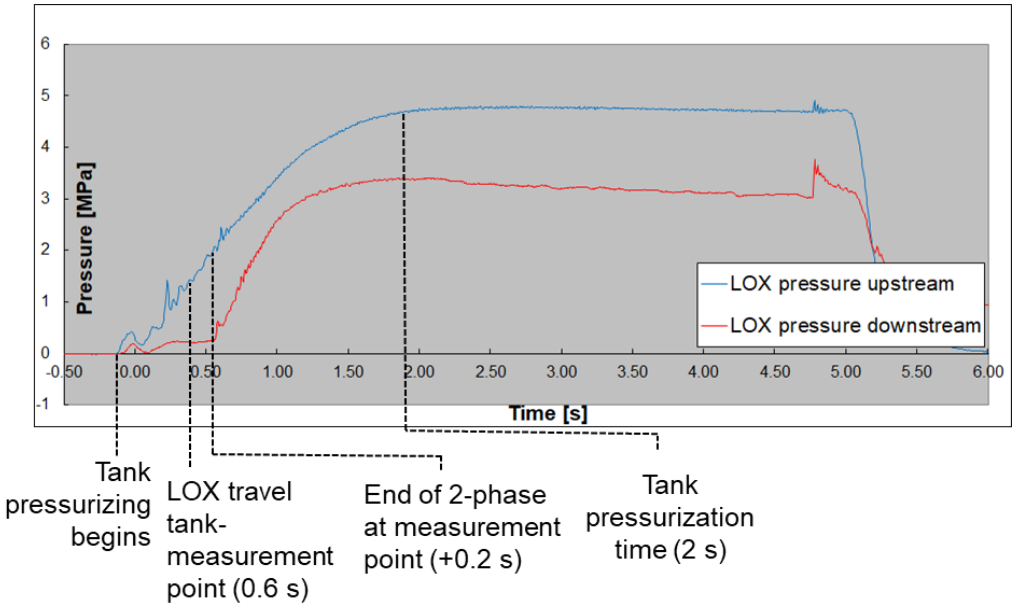

Figure 4.4: TTY04 LOX line pressure graphs.

given by Eq. (4.9):

$$t_{t2ph} = \frac{500 \cdot (283 - 150) \cdot 7930 \cdot 8.4 \cdot 10^{-5} \cdot 1.5}{920 \cdot (150 - 90) \cdot 1 + 214 \cdot 10^3 \cdot 1 \cdot 0.3} = 0.6s. \tag{4.9}$$

Looking at the terms separately, we get the following:

Tank to measurement point = 0.2 s.

Measurement point to engine = 0.4 s.

The typical test burn times have been between 2 s and 10 s, this gives a potential LOX flow error before the flow has stabilized in the flow-line until the measurement point, of $\approx 1 - 5\%$. Similarly, this gives a potential LOX flow error before the flow has stabilized in the entire flow-line (until the injector), of $\approx 2 - 10\%$.

Tank pressurization time

From the upstream pressure measurement shown in Figure 4.4 the tank pressurization time is deduced. This time is defined as the time from the start of pressure rise to the time 90% of maximum pressure is reached. In the case of the TTY 04, the re-pressurization time is around 2 s. For the rest of the TTY series firing tests, this varies from 1-2 s.

Time of ignition flame spreading

Using Eq. (4.3), the TTY04 flame spreading time becomes Eq. (4.10):

$$t_f = \frac{0.0107 \cdot 10}{1} = 0.1s. \tag{4.10}$$

The typical test burn times have been between 2 s and 10 s, giving a potential burn time error of $\approx 1 - 5\%$.

Local burn surface gasification

The analyzed TTY engines show 28 separately calculated burn surfaces and an average O/F ratio of around 2. This gives an approximation of $\approx 1 - 2\%$ potential error for the propellant mass flux. For the O/F ratio, this results in the $\approx 2 - 50\%$ potential error caused by the local fuel gasification. It is important to note that the uncertainties will be most significant at the upstream surfaces and diminishes the further downstream the surface is.

Re number

Based on the values reported in Ref. (11), the *Re* values from the RIE test series show a shift of m exponent from 0.8 to 0.6, giving a potential m exponent error of up to $\approx 30\%$.

Model assumptions

With the simulation done with the first fuel block upstream end-face forced to fit the measurements, the performance of the regression simulator for TTY04 is as shown in Fig. 4.5.

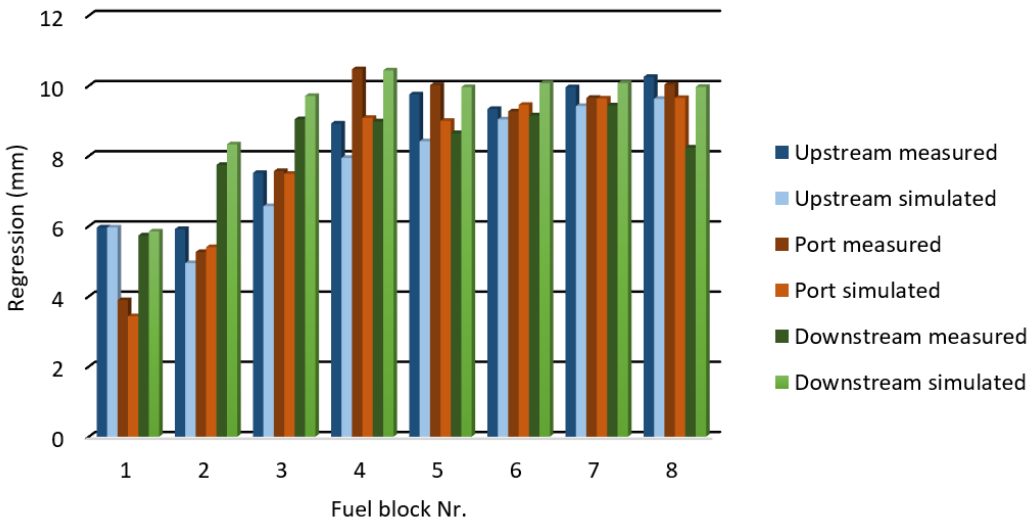

Figure 4.5: Corrected regression simulator error distribution (TTY04).

When compared to Fig. 4.3, the errors of the downstream burn surfaces are reduced considerably from up to 43% error to no larger than 21% with average error values (normalized) going from 19% to 9%.

4.3.2 Regression simulator sensitivity

For the identified potential errors, LOX flow, burn time, propellant mass flux, O/F ratio and m exponent, the sensitivity of the simulator are shown in Figs. 4.6 to 4.10.

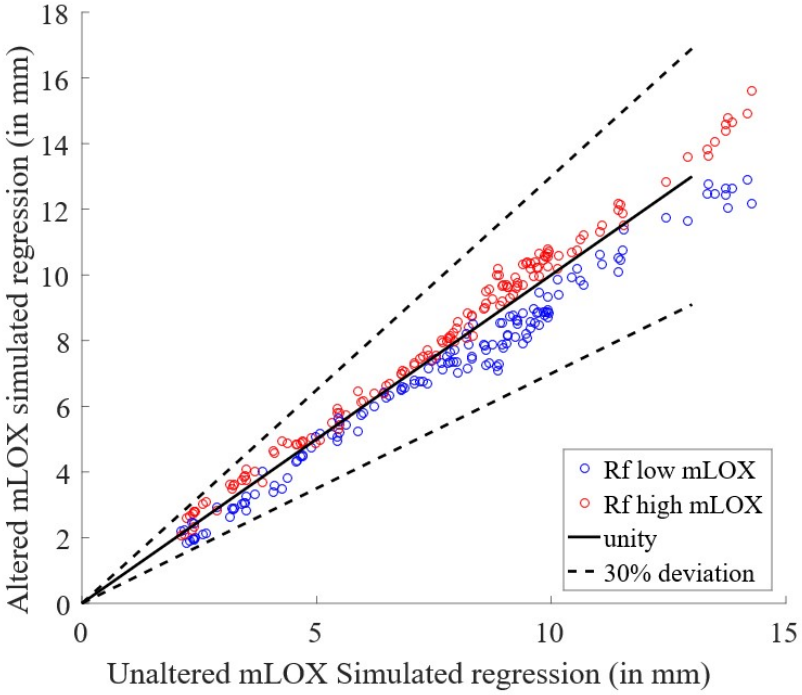

Figure 4.6: Sensitivity to LOX flow ±30%.

4.3.3 Results summary

The analyzed uncertainties and their potential effect on the regression simulator are summarized below in Table 4.4.

The results shown in Table 4.4 indicate that the largest potential simulator errors are found in:

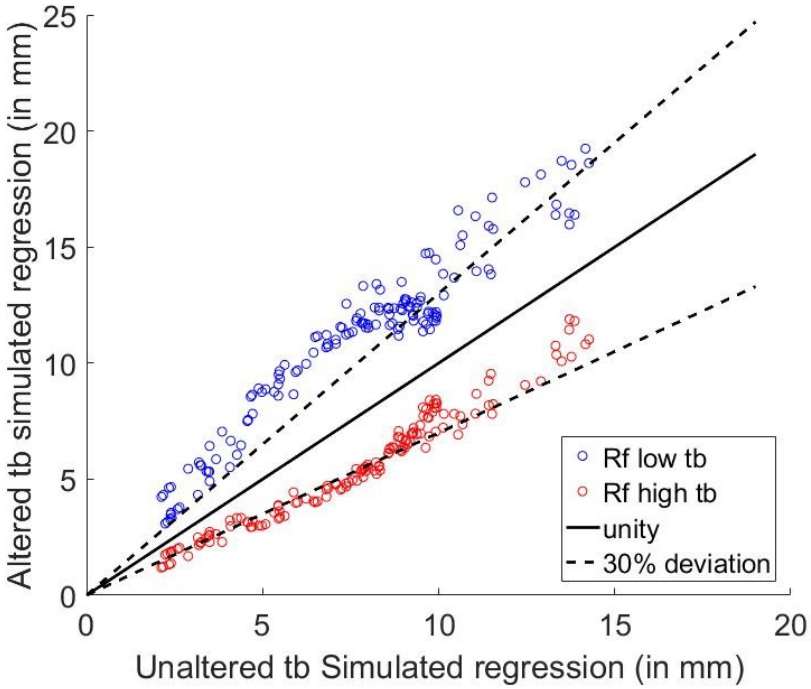

Figure 4.7: Sensitivity to burn time ±30%.

- LOX travel time
- local fuel gasification
- Reynolds number grouping
- model assumptions for the first upstream end face

It was also seen that overall burn time error overall had a disproportionately large effect on regression simulation error.

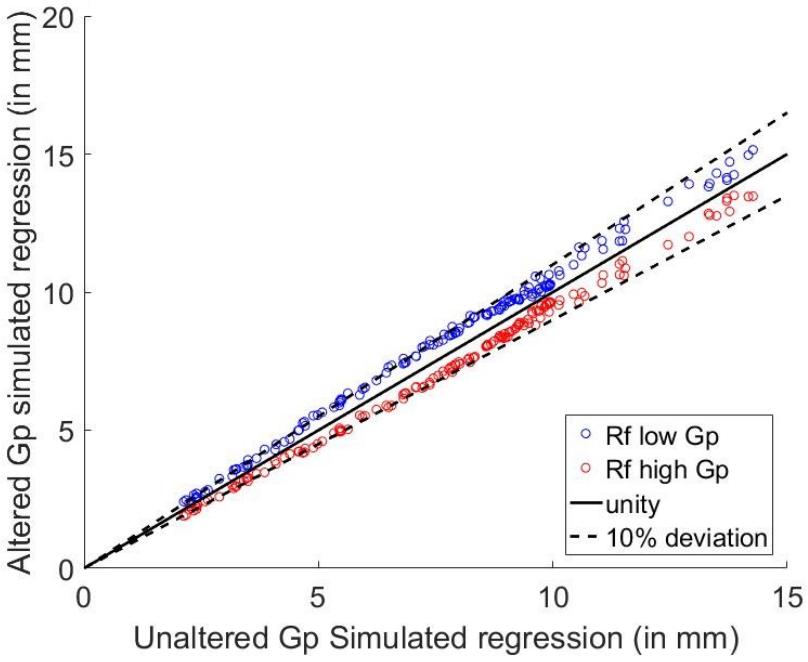

Figure 4.8: Sensitivity to propellant mass flux ±10%.

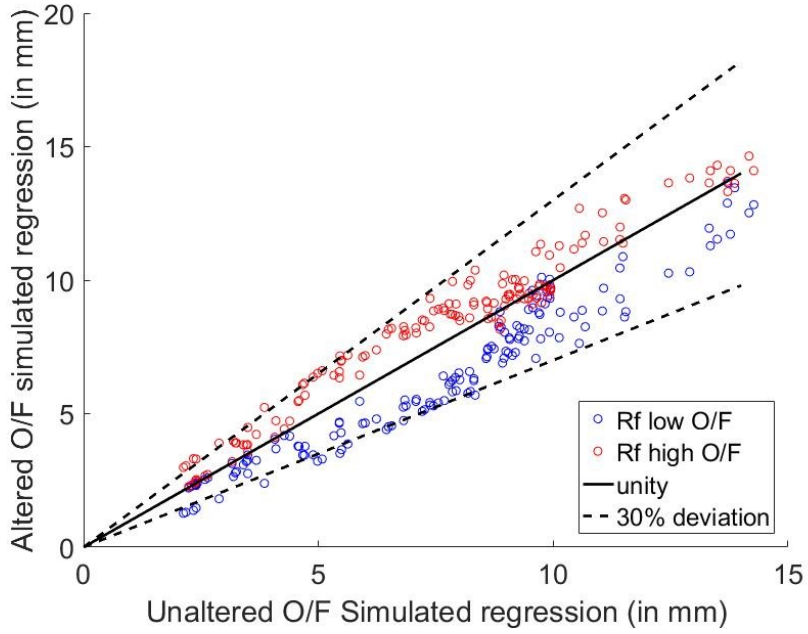

Figure 4.9: Sensitivity to O/F ratio ±30%.

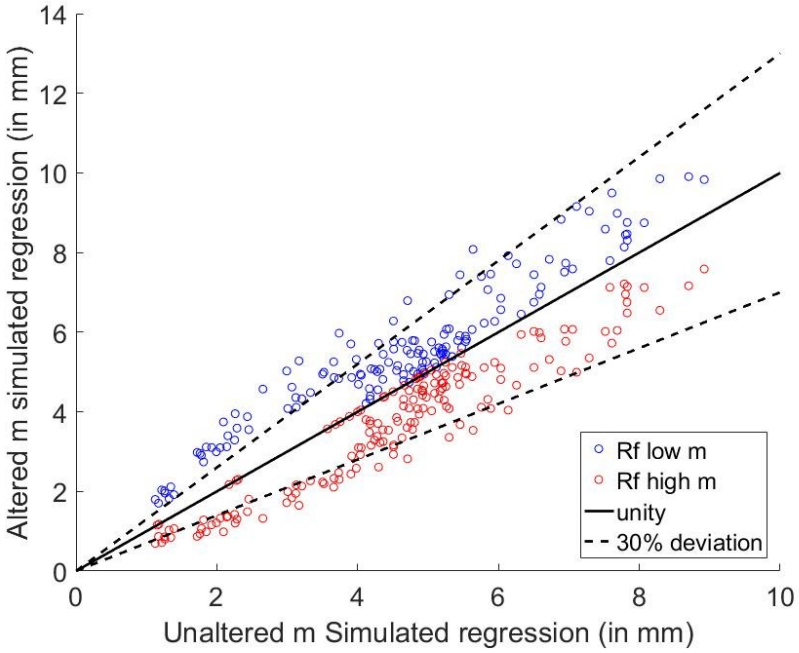

Figure 4.10: Sensitivity to m value $\pm 30\%$ (RIE).

Table 4.4:: Simulator regression uncertainties.

Uncertainty	Effected input	Input error in %	Simulator error in %
2-phase flow	LOX flow	$\approx 1-5$	$\approx 0-2$
2-phase flow	Burn time	$\approx 2-10$	$\approx 1-20$
LOX travel time	LOX flow	$\approx 5-25$	$\approx 2-10$
LOX travel time	Burn time	$\approx 10-50$	$\approx 5-100$
Flame spreading	Burn time	$\approx 1-5$	$\approx 0.5-10$
Local fuel gasification	Propellant mass flux	$\approx 1-2$	$\approx 0.5-2$
Local fuel gasification	O/F ratio	$\approx 2-50$	$\approx 0-50$
Re grouping RIE	m exponent	$\approx 0-30$	$\approx 0-60$
Model assumptions	Regression 1.st upstream block 1	$\approx 1-100$	$\approx 1-80$

Chapter 5

Uncertainty reduction

Based on the uncertainty mentioned above, corrections were made to the test setup for future firing tests and to the regression simulator. The corrections focused on here were the following:

- Inclusion of local fuel gasification
- Reduction of transient time during firing
- Burn time correction from long transient times

Each of these will be addressed in the following sections.

5.1 Inclusion of local fuel gasification

Previous research has used the regressed fuel mass from the previous burn surface to calculate the O/F and Gp values for a given burn surface. For the upstream end face

this is illustrated in Figure 4.2 (left). As mentioned in (9), the actual case is that local gasification for the surface that we are trying to calculate also influences these values. This is illustrated in Figure 4.2 (right).

To mitigate the potential errors that this can cause in the model, as described in (9), local fuel gasification is implemented into the regression model for the calculations of Gp and O/F by using the calculated regression from the earlier time step. This is illustrated in Figure 5.1.

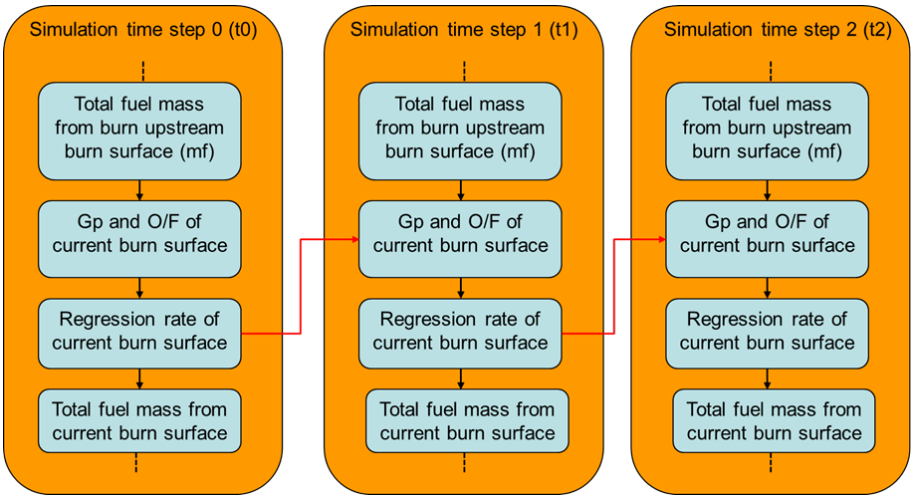

Figure 5.1: Local fuel gasification inclusion.

With $t1$ being the simulated time step calculated and $t0$ being the previous time step, this becomes for the upstream end face as follows:

$$G_p(t1) = \frac{(m_p(t1) + m_p(t0))}{(2A_p(t1)} \tag{5.1}$$

$$Xi_u(t1) = \frac{\dot{m}_{LOX}(t1)}{(m_u(t1) + m_p(t0))} \tag{5.2}$$

This is implemented similarly for the downstream end face and the port.

5.2 Reduction of Transient Time During Firing

As discussed in (9), the effect of an uncertain burn time has a significant adverse impact on the simulated regression accuracy. One of the ways to minimize this uncertainty is to reduce the start-up transient during firing. To investigate this effect, several firings were performed with different feed conditions to control two of the critical causes of start-up transient of the CAMUI engine: the LOX tank pressurization time and the 2-phase flow.

Additional LOX valves were included in the test setup to control the LOX tank pressurization time and allow for pre-cooling of the feedline without cooling the injector faceplate. These are shown below in Figure 5.2 as OMV1 and OMV2. The injector faceplate must not be cooled as the o-ring used to seal it to the combustion chamber was not rated for cryogenic temperatures.

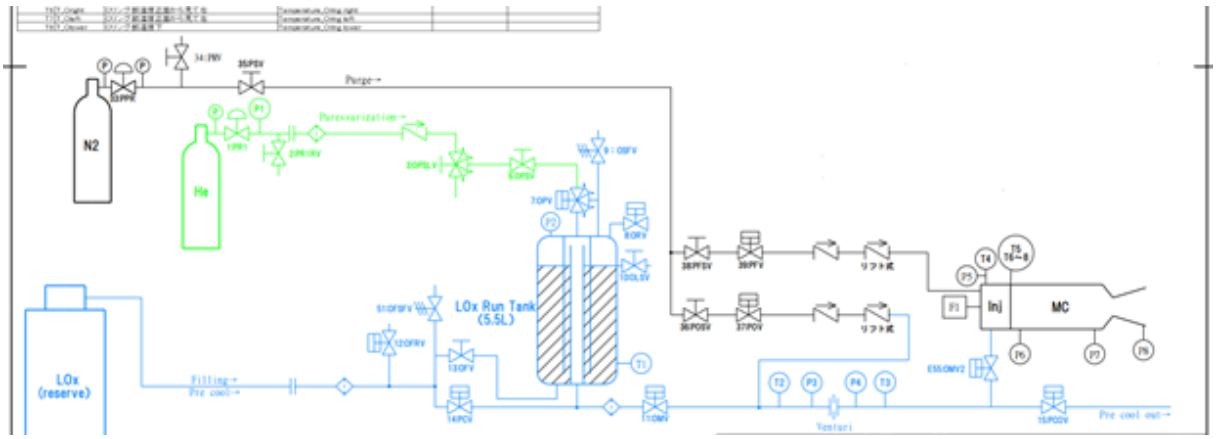

Figure 5.2: Transient investigation test setup.

To test the effect of pre-cooling and pre-pressurization on the LOX flow profile and the injector plate's temperature, the injector plate itself was attached, and LOX flow was done as if during firing. The total amount of LOX that flowed was the full tank. All four tests were performed using a fan-shaped injector head. The sequence of the tests where:

Test 1 (pre-pressure, no pre-cooling)

1. LOX tank filled
2. Feed pressure applied to LOX tank
3. OMV1 opened
4. OMV2 opened
5. LOX flow run until tank empty

Test 2 (pre-pressure, feed-line pre-cooled)

1. feed-line cooled
2. LOX tank filled
3. Feed pressure applied to LOX tank
4. OMV1 opened
5. OMV2 opened
6. LOX flow run until tank empty

Test 3 (no pre-pressure, feed-line pre-cooled)

1. feed-line cooled
2. LOX tank filled
3. OMV1 opened

4. OMV2 opened

5. Feed pressure applied to LOX tank

6. LOX flow run until tank empty

Test 4 (pre-pressure, feed-line and injector pre-cooled)

1. feed-line and injector cooled (until injector manifold reaches -50 degrees as from MSS 01)

2. Feed pressure applied to LOX tank

3. LOX tank filled

4. OMV1 opened

5. OMV2 opened

6. LOX flow run until tank empty

The resulting LOX flow from the four tests can be seen in Figure 5.3.

The MSS series was designed based on the analysis data from the RIE test series. They were not made to be scaled versions, and geometric proportions are not the same. Of the four tests, it seems test 2, which includes pre-cooling of the feed-line and pre-pressurization, gives the fastest steadying of the LOX flow.

It is important to note that the stabilization would look different during a firing. Still, the comparison between the four methods would be expected to be similar during actual engine firing. Test 4 was performed to confirm the theory of the overcooled injector

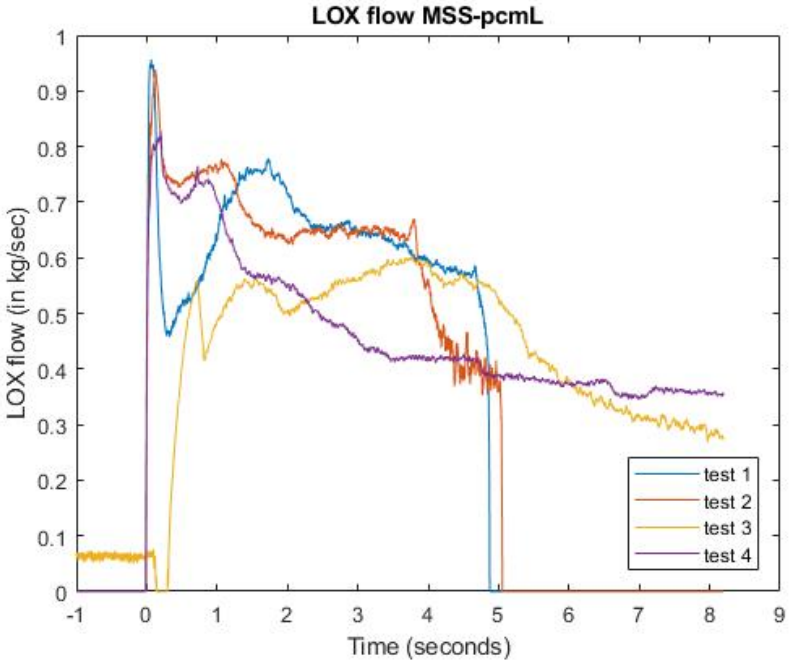

Figure 5.3: LOX flow test.

faceplate regarding a failure that happened at the firing of MSS 01. This failure showed a burn-through at the o-ring of the injector manifold. The injector faceplate temperature for tests 1-4 is shown in Figure 5.4, where it can be seen that the temperature does not decrease dramatically during the firing/LOX flow time. It is also clear that at the time of the firing, the injector manifold (at -50 degrees) and the injector faceplate are below the minimum temperature rating of the O-ring. Pre-cooling of the injector and its resulting cooling of the injector O-ring is therefore assumed to be the failure cause of MSS 01.

Furthermore, it can be seen from Figure 5.4 that, even without the heat of a burning engine to balance the cooling from the LOX flow, the temperature of the injector faceplate and therefore, the injector O-ring will not reach the lower limit even during extended firing.

As a safety precaution, the injector plate design was changed to be epoxy bonded

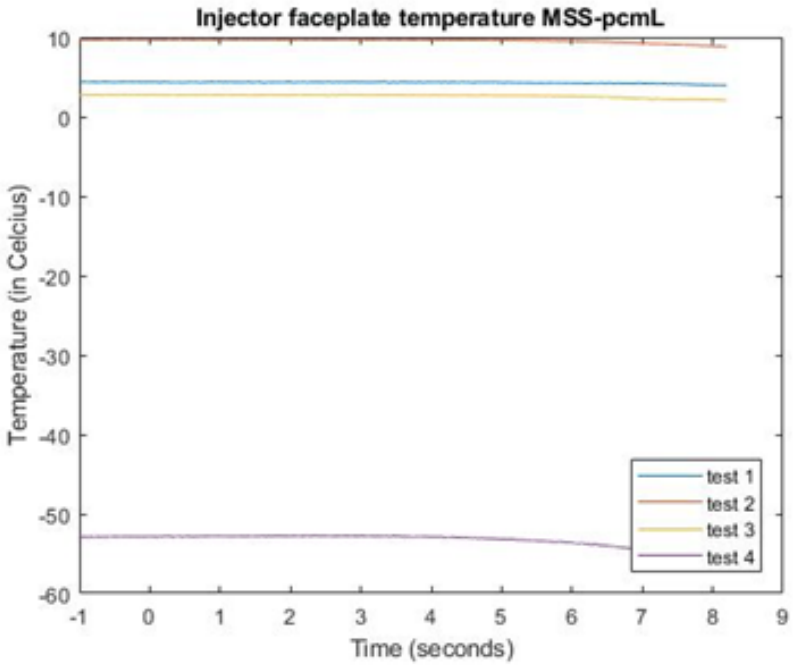

Figure 5.4: Injector faceplate temperature.

to the combustion chamber (over a large surface area) instead of relying on an O-ring. Though no O-ring was used in the injector plate for MSS 02, it was still deemed risky to pre-cool the injector as this could also affect the epoxy bonding between steel and GFRP. It is therefore for now recommended to avoid pre-cooling of the injector plate.

As the goal is to minimize start-up transients, the feed and start-up sequence of LOX test 2 was decided to be used for the MSS 02 engine firing. This means that the LOX feed-line was pre-cooled (until OMV2), and the tank and LOX feed-line were pre-pressurized (until OMV2).

The MSS 02 engine firing procedure was as follows:

1. feed-line cooled
2. feed-line purged with gaseous N2

3. feed pressure applied to LOX tank

4. OMV1 opened

5. engine igniter is powered ($t0$ -10 sec)

6. OMV2 opened ($t0$)

7. OMV2 close ($t0$ +10 sec)

8. chamber purge ($t0$ +10 sec)

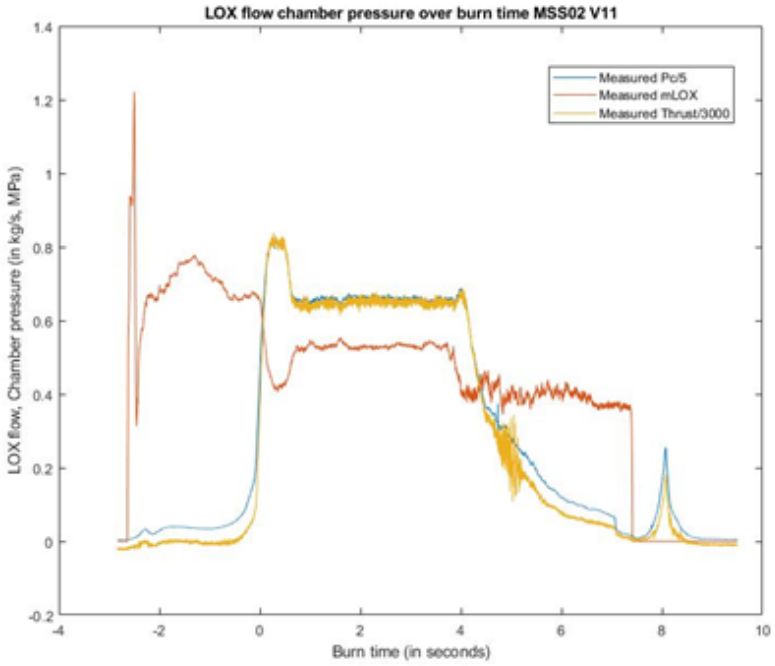

Figure 5.5: MSS 02 firing.

As can be seen in Figure 5.6, for most of the surfaces, the measured regression is higher than expected from the simulations. It is important to note that the MSS series was not designed to be a scaled version of the RIE, though the analysis of the RIE data was used to design the MSS fuel. This means that similarity conditions can not

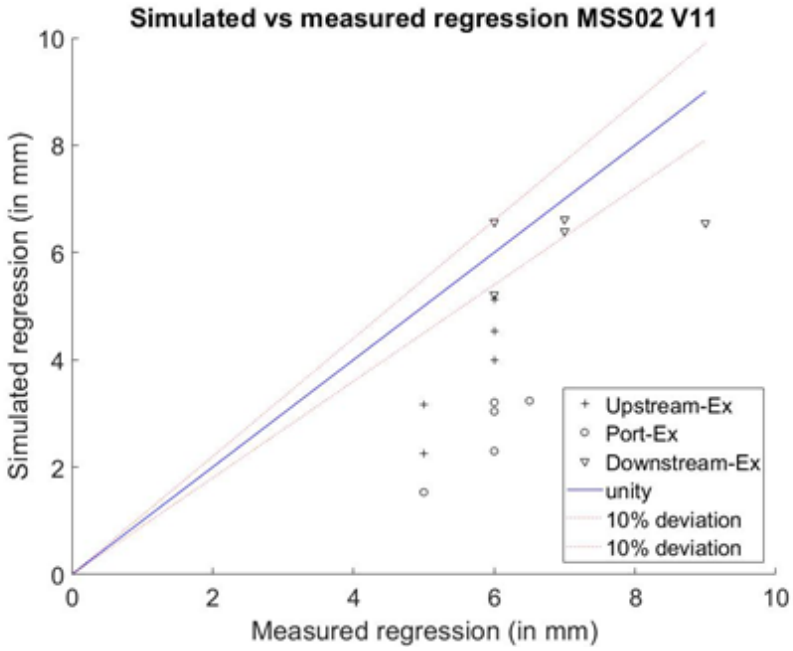

Figure 5.6: Simulated vs measured regression MSS02.

be expected to be valid, which is likely a big reason for the large discrepancy between simulated and measured regression.

Another big reason for the discrepancy is believed to be the effect of very different start-up transient times between the RIE series and the MSS series. This will be further investigated in Section 5.3.

5.2.1 Ignition delay

The cause for the ignition delay seen in Figure 5.5 is not yet known. It is seen as highly unlikely that there was a 10 seconds delay in igniting the gunpowder-epoxy used as ignition material. This mixture was believed to ignite, but as the feed-line had been purged with N2, N2 would also be the first gas hitting the igniting surface and possibly extinguishing it. As the ignition system is a continuously heating wire with chemical

propellant (epoxy gunpowder), this would mean that even if extinguished by the N2, it would then reignite once oxygen replaced the N2. To verify this, the next test was done under identical conditions, but purging the feed-line with GOX instead of N2.

5.2.2 Starting pressure peak

The reason for the 0.5-second initial pressure peak is believed to be linked to the extinction and reignition of the igniter caused by the N2. This would cause a large amount of 100% unburned combustible gas generated by the lack of oxidizer in the mix, igniting once the oxygen arrives. This, though, is speculation and was not further investigated apart from verifying that when purging the feedline with oxygen instead of with N2, this phenomenon did not happen.

5.2.3 Post combustion peak

The reason for the post-combustion peak was not further investigated. Four additional firing tests, MSS03-MSS06, were then performed, which were used to further evaluate the start-up transients.

5.2.4 MSS03

The startup conditions for MSS03 were as follows: the feedline until the main valve (V02 in Figure 3.3) was pre-cooled using LOX. The feed-line was subsequently purged with GOX, whereafter the LOX tank and feedline until the main valve (V02) was then pre-pressurized. MSS 03 was successfully fired with a 7 second burn time with a nominal

burn. Burn time was extrapolated from the fuel regression for the next test. Based on this, it was decided to use 13 seconds burn time for MSS 04.

Figure 5.7: MSS 04 fuel after firing.

5.2.5 MSS04

The startup conditions for MSS04 were as follows: no cooling of the feedline was performed. The LOX tank and feedline until the main valve (V02) was pre-pressurized. MSS 04 was successfully fired for 13 seconds with a nominal burn. This fits very closely with the optimal burn time before burn-through of the fuel blocks. Based on this, 20 seconds was estimated for a complete burn-through of all fuel surfaces. This was decided to be used for MSS 05. Figure 5.7 shows the residual fuel from MSS 04.

5.2.6 MSS05

The startup conditions for MSS05 were as follows: no cooling of the feedline was performed. The LOX tank and feedline until the main valve (V02) was pre-pressurized. MSS 05 was successfully fired for 20 seconds with a nominal burn. At this burn time, all fuel end faces had burned through. At this point, some softening of the fuel block slivers was observed, and a small sliver was ejected out the nozzle with no blockage or damage to the nozzle. These slivers are shown below in Figure 5.8. Structural collapse of the basic CAMUI fuel was observed, though with no negative effect on the engine performance or stability. This is believed to be caused by the collapse being very late in the burn and being caused by the softening of the fuel blocks and not by cracking or breaking. This means the fuel slivers stay for the most part inside the engine and continue to burn nominally. This can be seen in more detail in Figure 5.8 (right).

Figure 5.8: MSS 05 fuel after firing.

5.2.7 MSS06

The start-up conditions for MSS06 were as follows: no cooling of the feedline was performed. No pre-pressurization of the tank or feedline was performed. MSS 06 was

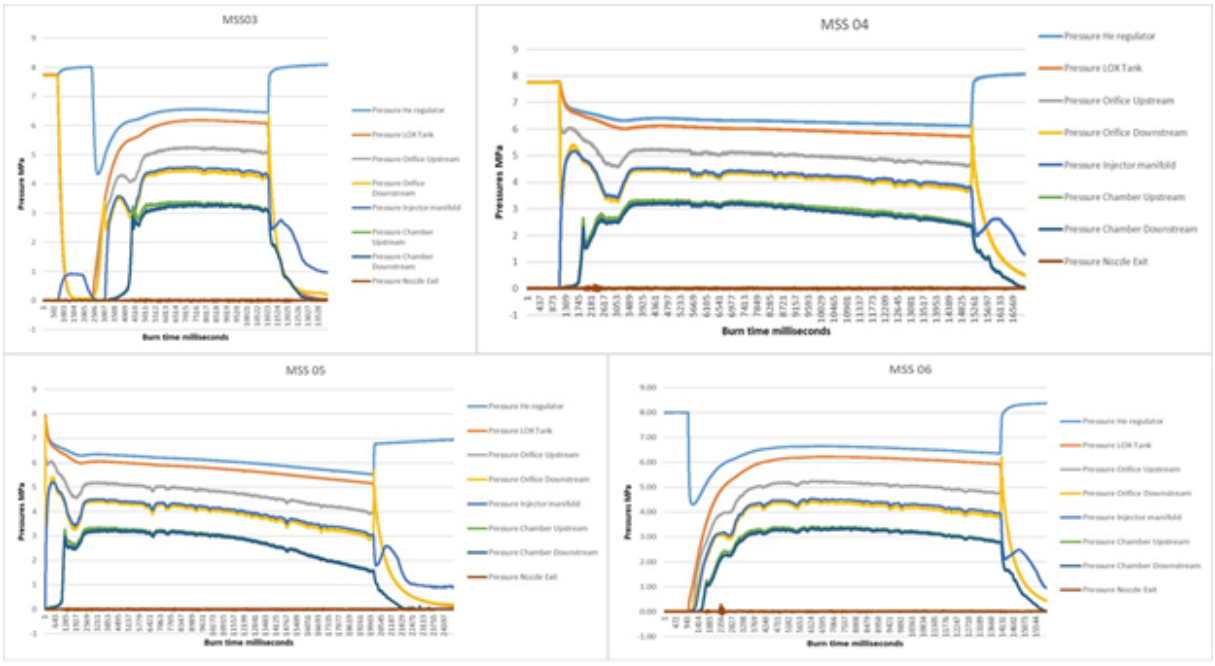

Figure 5.9: MSS03-06 pressure curves.

successfully fired for 10 seconds with a nominal burn. This firing also completed the last of the start-up sequence testing. It is worth noting that none of these follow-on tests exhibit the initial peak shown in MSS02. This supports the hypothesis that the peak was caused by the abnormal ignition conditions caused by the N2 purging of the feedline before firing.

5.2.8 Transient time reduction

Compared with a typical graph of the TTY series as shown in Figure 25, the transient times of the MSS engines have been considerably reduced from around 2 seconds to about 0.5 seconds, with the exception being the MSS06 which, as expected, had a transient of roughly 2 seconds. This is despite pre-cooling of the feedline confirming that the main key transient effect comes from the LOX pressurization time. Figure 5.10 shows TTY 04

transient times.

Six additional firing tests were performed under this test series with both low Reynolds numbers and high Reynolds numbers fuel design to support the work of the burn time correction as described in the next section.

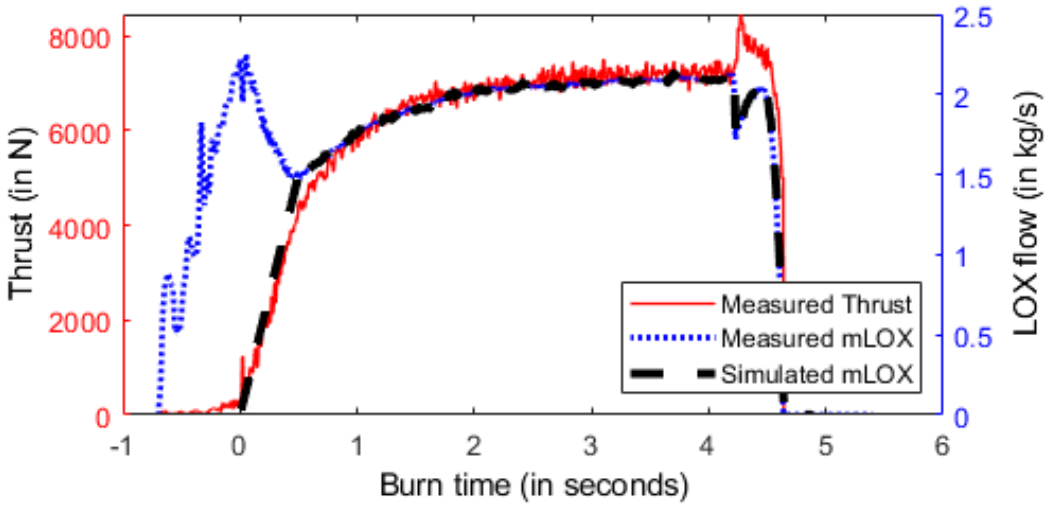

Figure 5.10: TTY 04 transient times.

5.3 Burn Time Correction

The reduction of transient time was a successful way of reducing the burn time uncertainties. This though did not help for existing firing data. To reduce the uncertainty on data that, for one reason or another, can not have the transient time reduced, for example, for existing data, a method to correct the burn time was developed. Comparing the previous firings of the RIE and TTY engines to the new short-transient long-burn time firings of the MSS series allowed for the development of this concept. This section describes this development and its results as also published in (12).

5.3.1 Problematic of start-up transient

The current regression model calculates the regression rate as the total measured regression divided by the burn time. This gives the averaged regression rate throughout the burn time and not the steady-state regression rate. In other words, the model assumes a perfect step function burn with no start-up transient. This though is not the case and in some engines, including most of the CAMUI engines fired, including the RIE and TTY test series, it takes 1-2 seconds for the burn to reach its steady-state. Using the TTY 04 engine data as an example, this effect is seen in Fig.5.10.

When this is compared to a burn time of 2-10 seconds typical of the CAMUI engine tests, a 2-second transient is a very significant time. Combined with the regression models' use of averaged values, such a start-up transient will cause an error in the empirically derived constants used in the model. As discussed in Section 4.3, the LOX flow measurement is not deemed reliable for the first half-second or so. Therefore, when using the measured LOX flow as the oxidizer flow rate in the simulator, the LOX flow during this time is changed to be linear rising LOX flow, from 0 seconds at the beginning of chamber pressure/thrust rise to the measured LOX flow at what is deemed the LOX flow measurement stabilization point. After that, the simulated LOX flow is the measured LOX flow. In this case, the simulated and actual measured LOX flow can also be seen in Fig. 5.10.

As described in Section 4.3, the existing model is very sensitive to burn time errors, with the resulting regression error reaching up to 60% for a 30% burn time error when looking at the TTY engine series. Fig. 4.7 shows this disproportionately large effect that the burn time error has on the regression accuracy. Combined, this gives a significant

potential error in the simulated regression accuracy. This fits well with the results of the uncertainty analysis performed by Frederick et al. (13) on the effects of start-up transients for traditional tube-shaped hybrid rockets.

It is important to note that where the liquid oxygen fuelled CAMUI has burn times same order of magnitude as the transient times, Frederick et al. (13) had transient times of an order of magnitude shorter than the burn times. Despite this, their research concluded that the start-up transients had the most significant uncertainty effect on the regression rate estimation. More recently, Cai et al. (14), presents an analysis of the length of the start-up transient and the impact of the local oxidizer flow rate on the start-up transient time. Their transient times span the range of around 0.2 seconds to over 1 second, which fits well with both the engines used by Frederick et al. (13) as well as the ones analyzed in this work.

Overall this is a strong indication that for CAMUI, the transient effect is potentially the most significant uncertainty in the regression model. This uncertainty disappears if the burn time is long enough compared to the transient time. But cutting the transient time down to 1-2 orders of magnitude shorter than the burn time can prove complicated. Secondly, large databases of existing firing data have relatively large transient times. For these reasons, the simulation model is adjusted to take this transient time phenomenon into account.

5.3.2 Equivalent burn time

Based on the regression simulator described in Section 2.3.3, equivalent burn time is defined such that, when used in the constants analyzer part of the CAMUI simulator, it

will give the corrected regression constants for the steady-state burning. To implement this, first, the total impulse of each firing is determined. The steady-state thrust ($F_{steadyState}$) is then determined by visually evaluating the thrust curve of the given firing and estimating when the start-up transient ends and the steady-state level is reached. As illustrated in Fig. 5.11, the equivalent burn time is defined as the firing time of the engine that would, at this steady-state thrust level, result in the before-determined total impulse. Mathematically this is done as shown in Eq.5.3.

$$t_{b_{eq}} = \frac{\int F dt}{F_{steadyState}} \tag{5.3}$$

Updating the constants analyser to implement this equivalent burn time accordingly, results in adjusted a and m values in Equations 2.8-2.10 which are more representative of the steady-state values rather than the time-averaged values. Overall, the results of

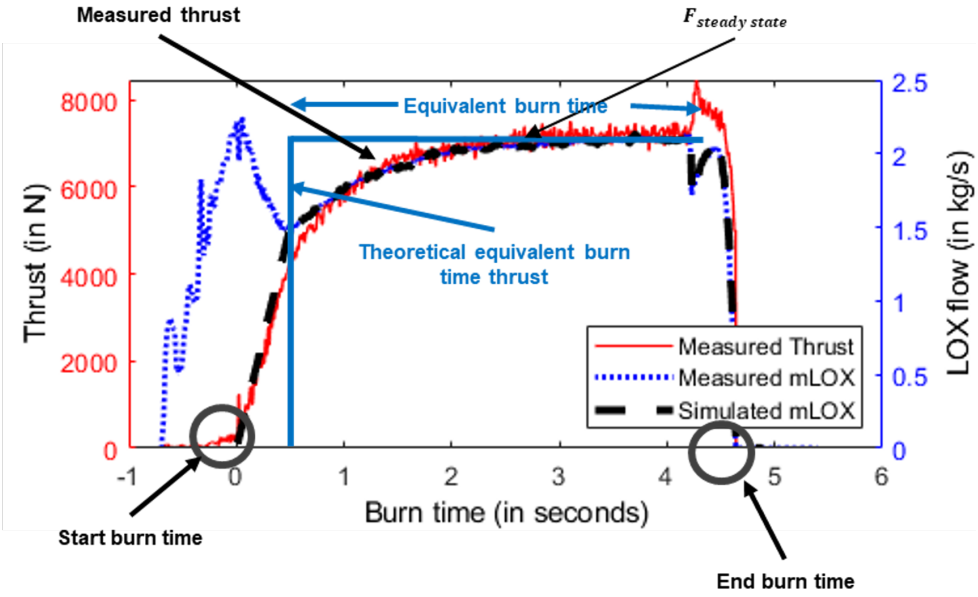

Figure 5.11: Equivalent burn time concept TTY.

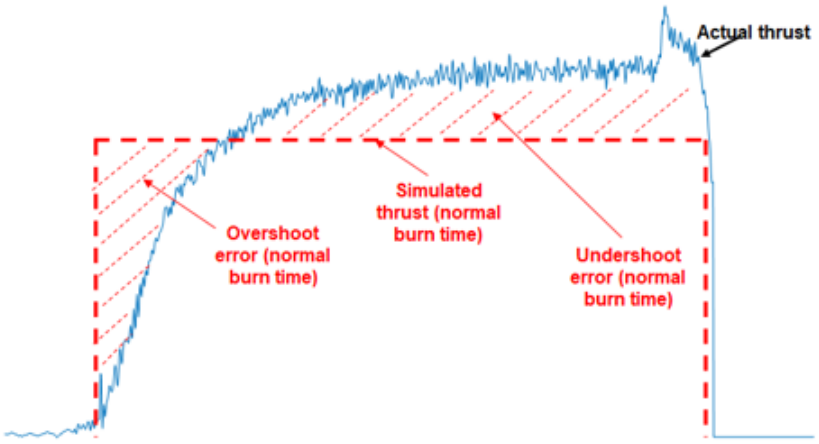

Figure 5.12: Overshoot and undershoot errors, using nominal burn time derived constants (conceptual)

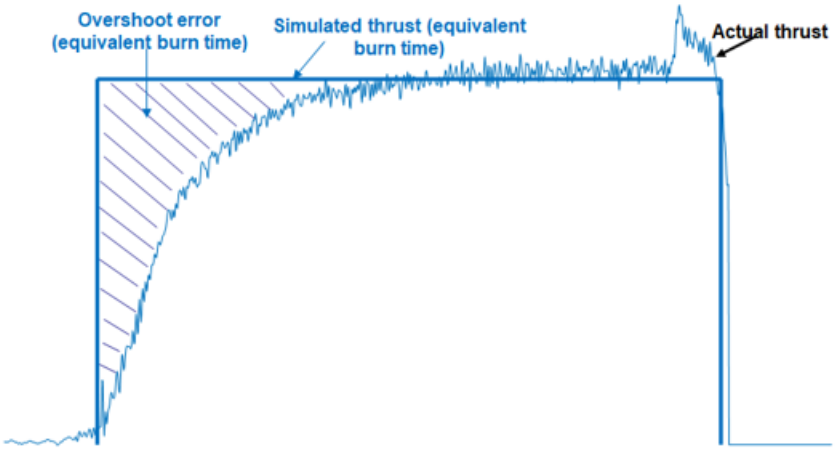

Figure 5.13: Overshoot error, using equivalent burn time derived constants (conceptual)

this are higher simulated regression rates and resulting thrusts.

To visualize how using these equivalent burn time derived constants compared to using the nominal burn time derived constants in the regression model changes the burn time error, the errors resulting from using nominal and equivalent burn times respectively have been illustrated in Figures 5.12 and 5.13. The regression simulations have been illustrated with an instantaneous step type steady-state LOX flow for better

visualization. As shown in Fig. 5.12, the error when using nominal burn time for the regression simulation is split into two regions. These are the overshoot region, where the regression rate is overestimated, and the undershoot region, where the regression rate is underestimated.

When simulating an engine similar in burn time and transient time to the engines used for derivation of the constants in the constants analyzer, the overshoot error and undershoot error of the nominal burn time will cancel out each other. If equivalent burn time is used in these cases, not only will the overshoot error be increased, but furthermore, the balancing undershoot error will be removed. This results in the simulated engine having an overall increase in the regression error. On the other hand, when the simulated engine has a longer burn time than the engines used for the constants analyzer for the derivation of the constants, the overshoot error stays the same while the undershoot error increases proportionally to the burn time. This results in the overall error in the simulated engine increasing. Once this increasing error becomes more important than the additional overshoot error caused by the equivalent burn time, it is, in theory, an advantage to using equivalent burn time.

In the same way, when the analysis engine has a longer transient time than the simulated engine, the undershoot error stays the same while the overshoot error decreases. Using equivalent burn time again becomes advantageous once the initial undershoot error becomes smaller than the decrease in the overshoot error.

To empirically investigate this, the regression is simulated with and without the use of equivalent burn time and the resulting values compared to the measured results. The oxidizer inputs are the measured LOX flows from the firing tests for these simulations.

The engine test series used in this analysis are shown below in Table 5.1.

Table 5.1:: Engines used in this research.

Engine name	**RIE**	**TTY**	**MSS-Lo**	**MSS-Hi**
number of fuel blocks per engine	10	10	7	8
Fuel outer diameter (mm)	100	230	200	200
Nominal thrust level (kN)	2.5	10	2	4
Burn times (s)	2-5	5-10	5-25	5-10
Burn time category	short	medium	long	medium
Re number $.10^4$	1-5	10-20	1-5	10-20

To minimize the potential error of dissimilar Reynolds numbers as described in Nagata et al. (11), the engines series have been grouped in high Reynolds number engines and low Reynolds number engines. The RIE engines are similar in Re number to the MSS-Lo engines, and the TTY engines are similar in Re number to the MSS-Hi engines. Therefore, the RIE-series firing data is used in the constants analyzer to simulate both the RIE engines and the MSS-Lo engines. In the same way, the TTY-series firing data engines is used in the constants analyzer to simulate both the TTY engines and the MSS-Hi engines.

Figure 5.14 depicts the different calculation flows when using nominal burn time (left) vs using equivalent burnt time (right).

For the cases where nominal burn time is used as shown in Figure 5.14 (left), the empirical regression constants $m, c1, c2, c3$, and $c4$ are found for the upstream, port,

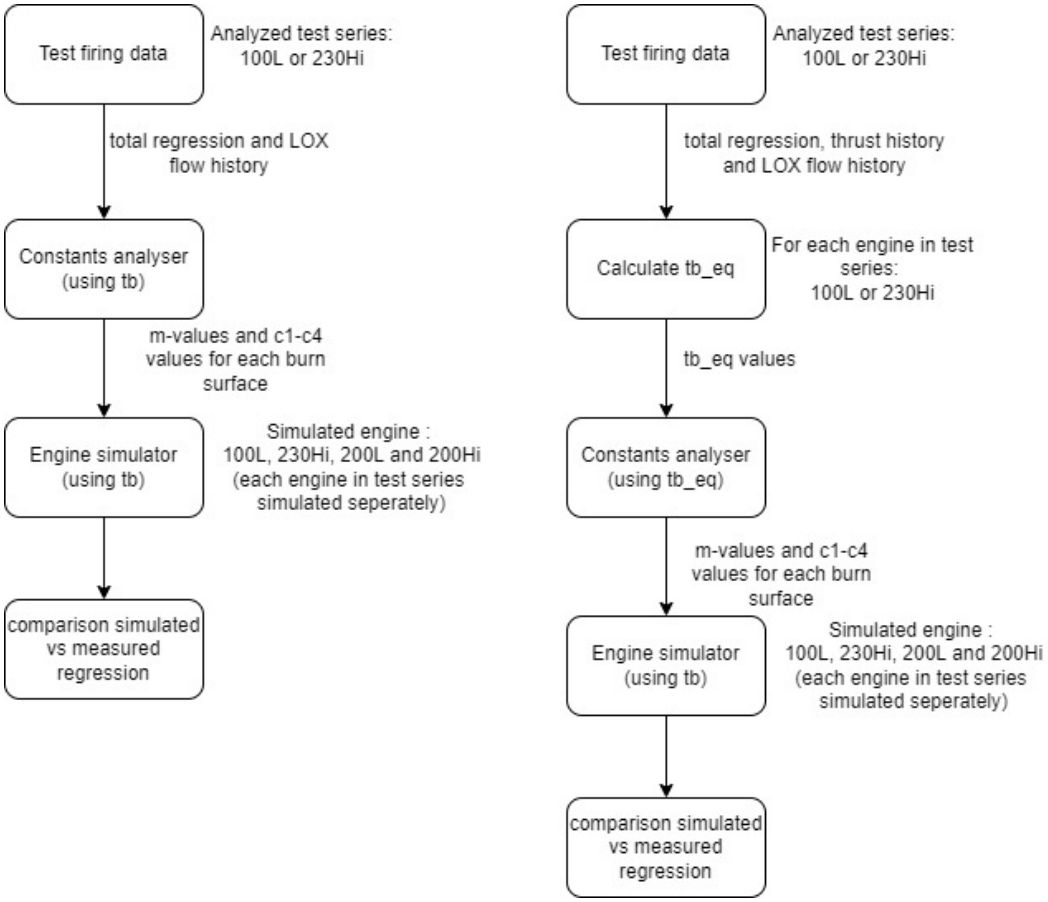

Figure 5.14: Calculation flow with nominal vs. equivalent burn times: when using nominal burn time (left), and when using equivalent burn time (right).

and downstream burn surfaces, respectively. The combined data from all firings in a given test series (RIE or TTY) are used for this step. These constants are then used for the regression simulation for each surface of each fuel block of any given engine of the investigated test series (RIE, TTY, MSS-Lo, MSS-Hi). Lastly, these individual surface total regression rates are compared with the measured ones. As shown in Figure 5.14 (right), when using the equivalent burn time, the equivalent burn time for each engine included in the constants derivation is calculated, according to Equation 5.3, before extracting the regression constants. The nominal burn times are then replaced by the

Table 5.2:: tb vs. tb_{eq} for RIE.

Engine Number	**1**	**2**	**3**	**4**	**5**	**6**	**7**
t_b	5.3	4.2	2.2	2.2	2.3	3	3.2
$t_{b_{eq}}$	4.7	3.5	2	2.1	2	2.6	2.6
% t_b reduction	11%	17%	10%	5%	13%	13%	19%

equivalent burn times (tb_{eq}) for the extraction of the empirical constants $m, c1, c2, c3$ and $c4$ for each of the three burning surfaces. These constants are then used for the regression simulation for each surface of each fuel block of any given engine of the investigated test series (RIE, TTY, MSS-Lo, MSS-Hi). This simulation is done using the nominal burn time t_b. Lastly, these individual surface total regression rates are compared with the measured ones.

5.3.3 Burn time correction results

The resulting difference between the original burn time and the equivalent burn time is illustrated below in Table 5.2 for the RIE test series and in Table 5.3 for the TTY test series.

The regression model performance for the port burn surface, when using RIE data as a baseline to simulate RIE engine firings, is shown in Fig. 5.15 (right). Here the performance for RIE data used as a baseline to simulate the MSS-Lo engines can be seen. Fig.5.16 (left) shows the performance for TTY data used as a baseline to simulate the TTY engines, and lastly, Fig. 5.16 (right) shows the performance for RIE data as a

Table 5.3:: t_b vs. $t_{b_{eq}}$ for TTY.

Engine Number	**1**	**2**	**3**	**4**	**5**	**6**	**7**
t_b	10.2	5.5	6.9	5.3	4.8	5	
$t_{b_{eq}}$	10	5.1	6	4.9	4.3	4.4	
% t_b reduction	2%	7%	13%	8%	10%	12%	

Table 5.4:: Simulated port regression error (RMS).

Analysis baseline engine	RIE		TTY	
Simulated engine	RIE	MSS-Lo	TTY	MSS-Hi
Error RMS t_b	15%	41%	14%	27%
Error RMS $t_{b_{eq}}$	47%	18%	24%	24%

baseline to simulate the MSS-Hi engines.

Calculating the port regression error RMS for simulated vs. measured regression for the same analysis and test firing scenarios, with and without the use of the burn time equivalent, results as shown in Table 5.4 are reached.

When considering all burning surfaces, Using the RIE data for analysis with and without $t_{b_{eq}}$ gives the RIE simulation results, as shown in Fig. 5.17 (left) and the MSS-Lo simulation results, as shown in Fig. 5.17 (right). Likewise, using the TTY data for analysis with and without $t_{b_{eq}}$ gives the TTY simulation results, as shown in Fig. 5.18 (left) and the MSS-Hi simulation results shown in Fig. 5.18 (right).

5.4 Uncertainty summary

Overall, it was shown that burn time transient could relatively easily be reduced from the typical 2 sec+, as in previous studies, to the 0.5 seconds achieved with an improved test set-up. Furthermore, for the situations where the test setup can not be designed to minimize burn time transient, the equivalent burn time showed to considerably reduce the uncertainties resulting from the start-up transients.

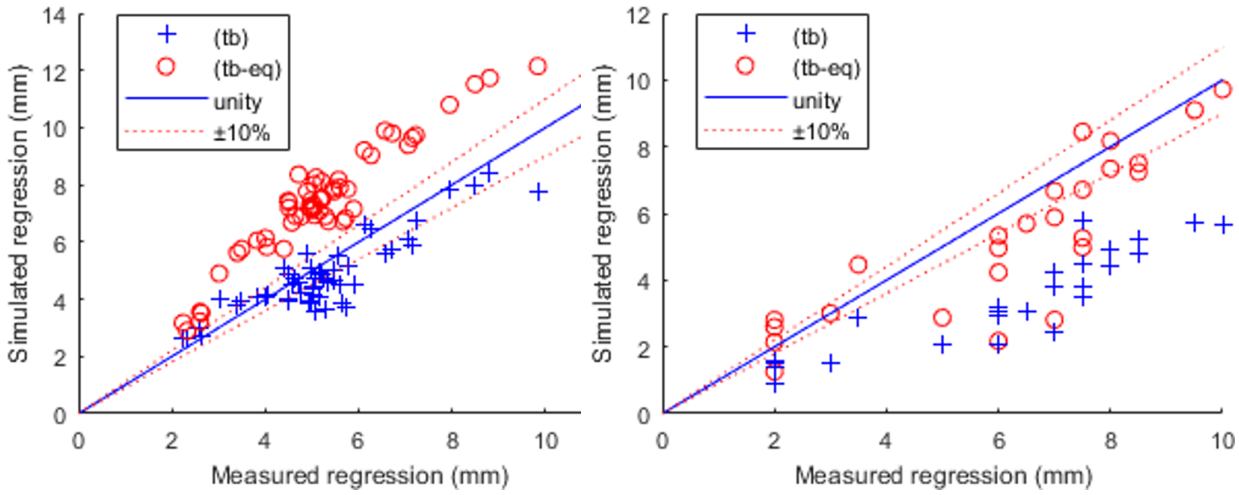

Figure 5.15: Accuracy of simulation for analysis of RIE engines using nominal t_b and $t_{b_{eq}}$, port only

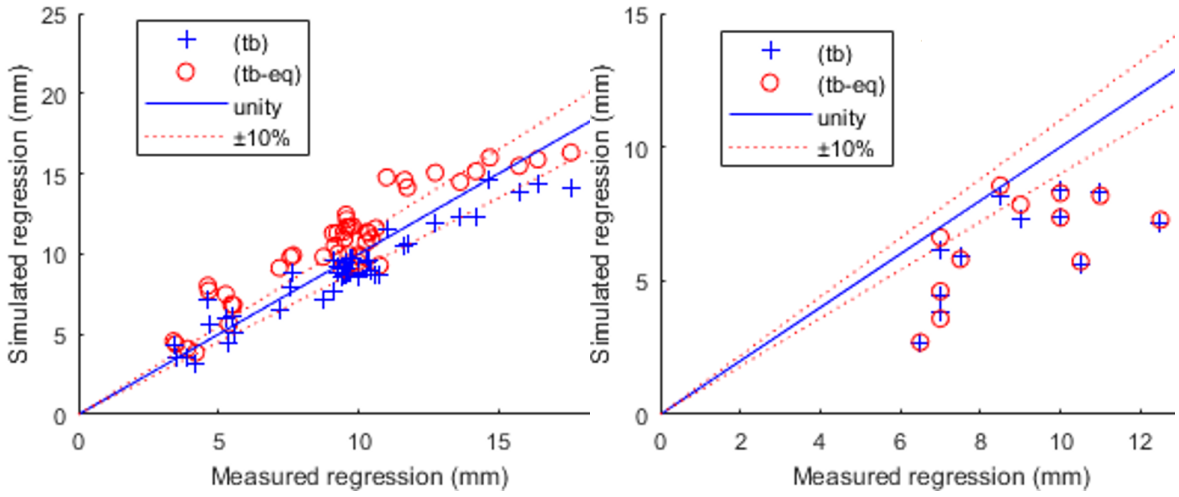

Figure 5.16: Accuracy of simulation for analysis of TTY engines using nominal t_b and $t_{b_{eq}}$, port only

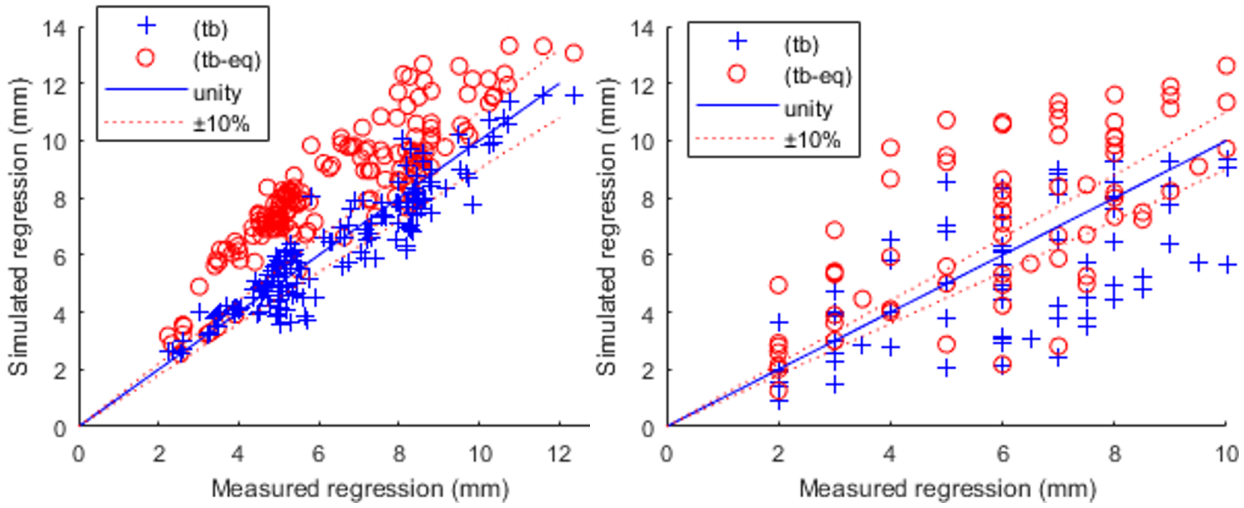

Figure 5.17: Accuracy of simulation for analysis of RIE engines using nominal t_b and $t_{b_{eq}}$

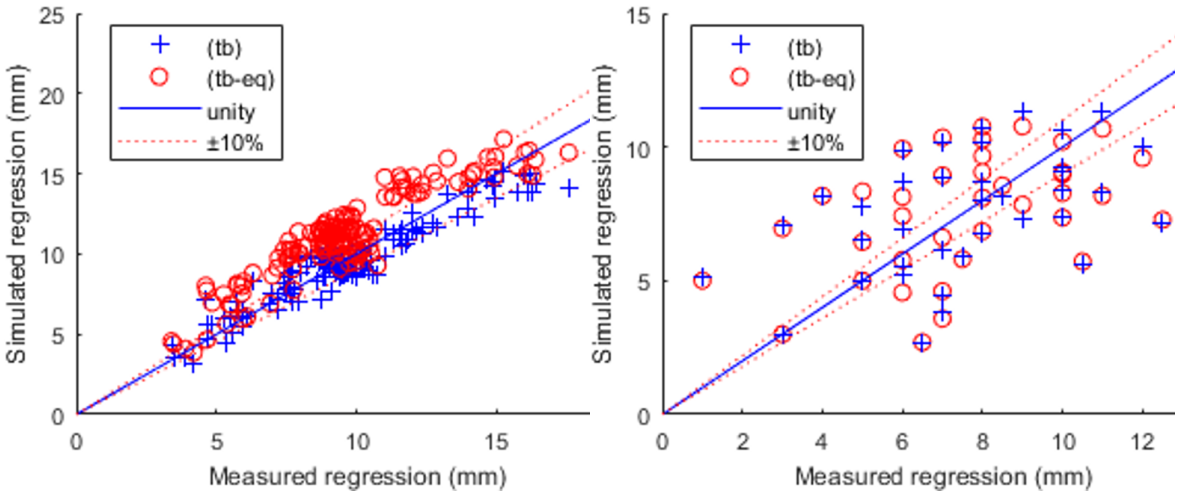

Figure 5.18: Accuracy of simulation for analysis of TTY engines using nominal t_b and $t_{b_{eq}}$

Chapter 6

Large scale engine development

The scaling of the 2 kN class to the 40 kN class was done in several steps, including an intermediate 8 kN test. This was due to uncertainty to the ignition transients, and from a scaling research point of view, the O-BASAN 40 kN class was scaled from the RIE and TTY test data. The final development step resulted in the successful firing of the 40 kN class O-BASAN 02 engine. This section provides a first evaluation of the scaling performance of the regression model with the corrections described in Section 5 as also published in (15).

6.1 First results

To evaluate the regression model baseline performance with the improvements described in Section 5, first, the RIE data is used in the constants analyser to extract the empirical values. The regression of each engine in the RIE series is then simulated and compared to the measured results. This is then repeated for the TTY series using the TTY series

data to extract the empirical constants used to simulate the regression of the individual engines in the TTY series to lastly be compared with the measured results.

Figure 6.1 shows the general performance of the model, using the RIE for analysis to simulate the same test series (left). Similarly, the results from using the TTY for the analysis to simulate the engines of the TTY series are shown in Figure 6.1 (right).

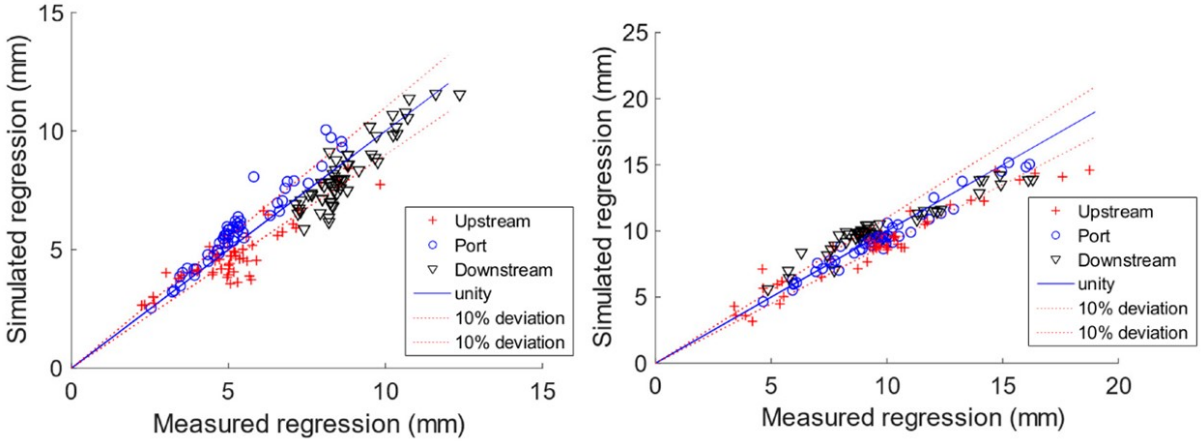

Figure 6.1: Model baseline performance for RIE (left) and TTY (right).

The calculated regression error RMS for simulated vs. measured regression are summarized in Table 6.1.

Table 6.1:: Model regression error RMS).

Motor Series	Error rms %
RIE	14.1
TTY	10.8

To evaluate the model's performance when used for scaled regression simulation, which is the model's primary purpose, the test data from the TTY series is analyzed and

used to simulate the fuel regression of the O-BASAN series. Lastly, to investigate the model scaling performance over a more extensive scaling range and different Reynolds numbers, the RIE test data is analyzed and used to simulate the fuel regression of the O-BASAN series. As before, the simulated regression is then compared with the measured regression giving the scaling performance of the model.

For this scaling performance of the model, using the TTY-series for analysis to simulate the fuel regression of the O-BASAN series, the results are shown below in Figure 6.2 (left). Similarly, the results from using the RIE for the analysis to simulate the fuel regression of the O-BASAN series are shown in Figure 6.2 (right).

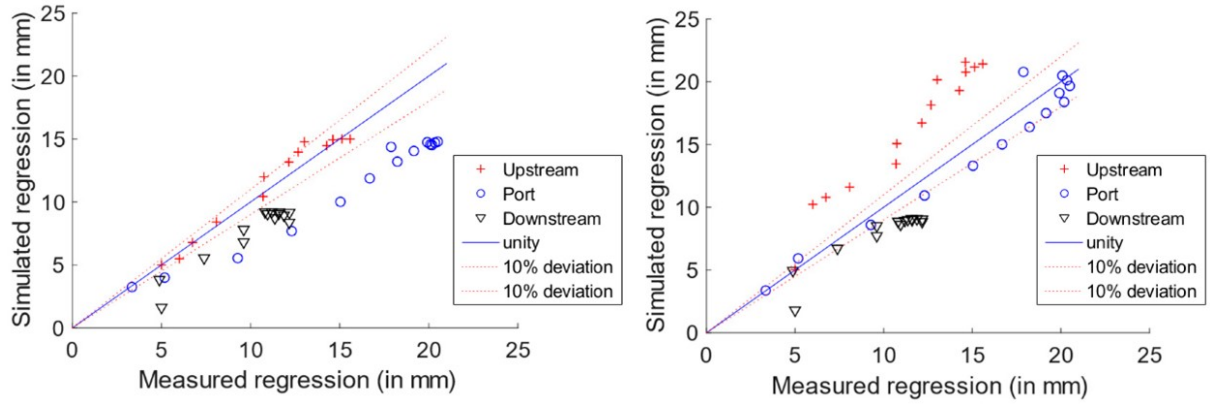

Figure 6.2: Model scaling performance for O-BASAN based on TTY analysis (left) and RIE analysis (right).

The calculated regression error RMS for simulated vs. measured regression are as shown in Table 6.2.

With the simulated regressions as described above, the simulated vs. measured O-BASAN thrust (normalized) is shown in Figure 6.3. Here the simulated I_{sp} has been corrected to have the two thrust curves overlap. This is done as the simulator calculates the regression only and not the combustion efficiency or the nozzle efficiency. It is

Table 6.2:: Scaled model regression error RMS.

Motor Series	Analysis Series Used	Error rms %
O-BASAN	TTY	22
O-BASAN	RIE	26

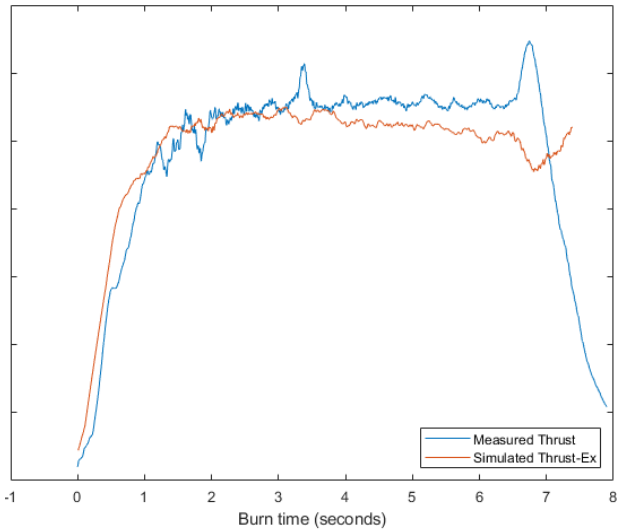

Figure 6.3: O-BASAN Thrust (Normalized)

important to note that the simulator assumes a constant I_{sp} and does not take into account the I_{sp}'s dependency on the O/F shift that occurs through the burn.

6.2 Fuel block measurement correction

As also mentioned in (15) one of the remaining sources of error in the scaled regression simulation performance from 6.2 is believed to be the original method of measuring the fuel blocks. These fuel blocks are no longer available so re-measuring them by other

methods is no longer an option. The original measurement points, though, are available. This section investigates a possible mathematical correction of these measurements. The original measurement method for the upstream end faces was done using three lines of point measurements done with a laser moving across the burn surface. The measurement points along a single line are taken with a fixed distance interval. The placement of these measurement lines are shown in Figure 6.4. Note this is only for the upstream end face.

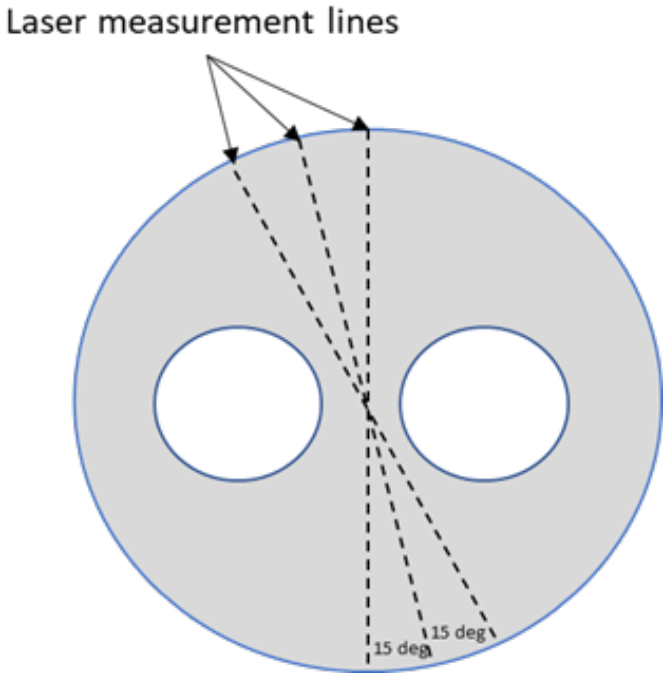

Figure 6.4: End face measurement line positions.

These are:

- Through the middle between the two ports (0 degrees)
- Angled 15 degrees compared to the first line
- Angled 30 degrees compared to the first line

The part of the central (0 degrees) line that overlaps with the area under the upstream fuel block ports is calculated. The measurement points from all three lines (0 degrees, 15 degrees, and 30 degrees) that have the same distance to the center as the above overlapping points are the measurement points taken into consideration in the averaging of the regression of the surface. This is shown in Figure 6.5. This causes a systematic error in that the weight of each measurement point is the same, but the area it represents increases the further away from the center point it is. This is illustrated in Figure 6.6. When looking at two sections with equal area, the section near the center point has considerably more measurement points/area than the area nearest the edge.

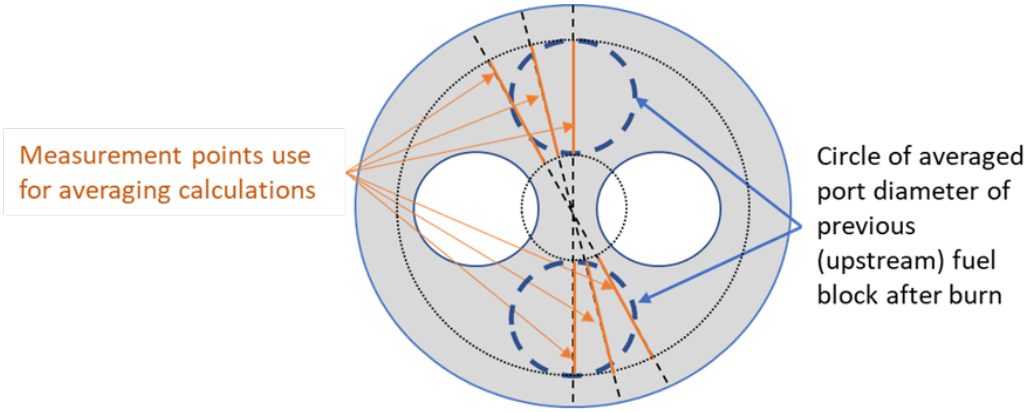

Figure 6.5: Averaging of measurement points.

6.2.1 Measurement Correction

To correct this, each measurement point can be considered to represent the area of a ring with a width of the distance between two measurement points as shown in Figure 6.7. With d being distance from centre to measurement point, each measurement point x is then weighted $x * d/d_{average}$. Lastly, whereas the previous measurements limited the areas used for averaging, the whole end face is measured in the current work.

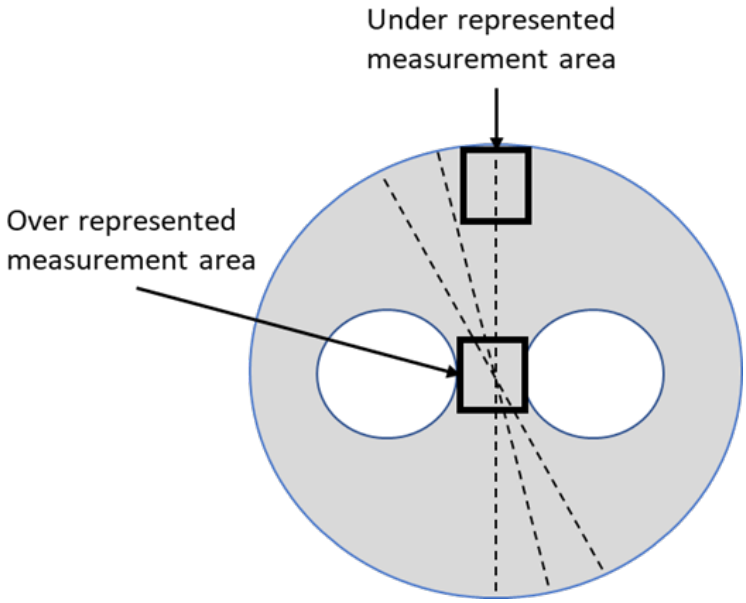

Figure 6.6: Over/under representation of measurement points.

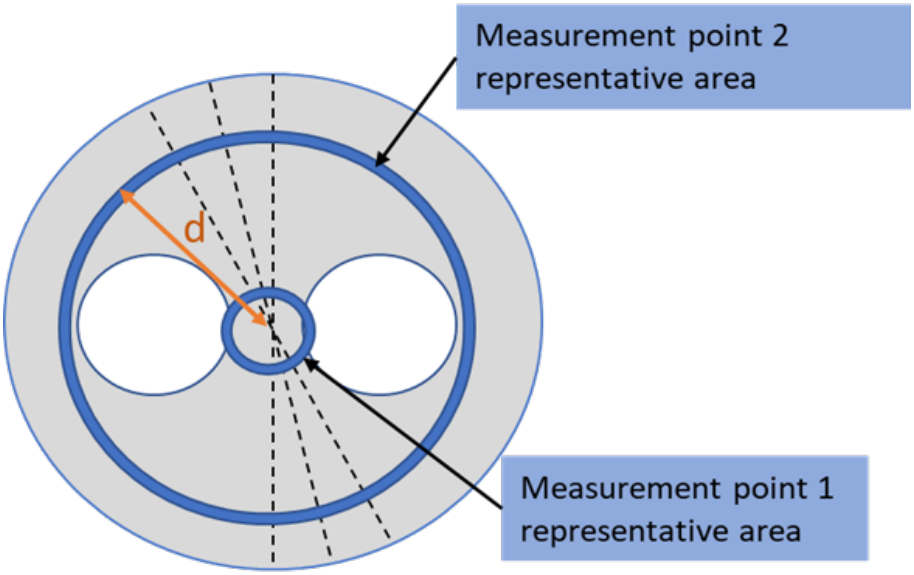

Figure 6.7: Ring representation of measurement points.

As can be seen in Figure 6.8, this gives a considerable difference. It is important to note that this error does in no way invalidate previous research. This is because the same method was used in all engines, and therefore the systematic measurement error

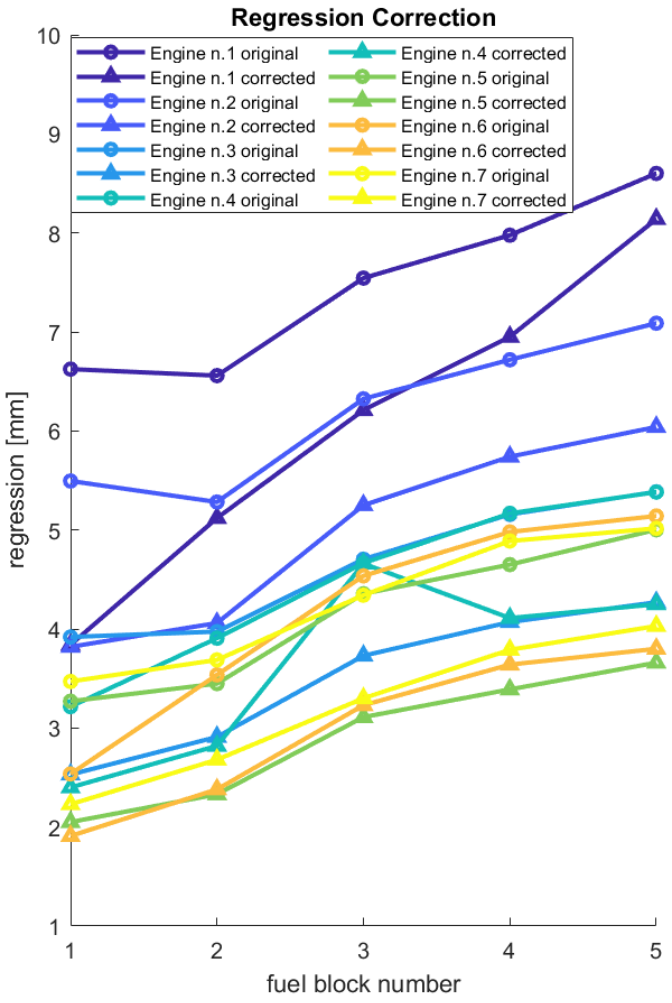

Figure 6.8: Upstream end face regression original and corrected values for each engine.

therefore largely balances out. On the other hand, this work has used two different methods and therefore is strongly affected by this error. The effects on the upstream regression performance when implementing this measurement correction are shown in Figure 6.9.

This shows a considerable decrease in the simulation error for the upstream end face when using the corrected fuel measurements of the 2.5 kN class RIE test series to

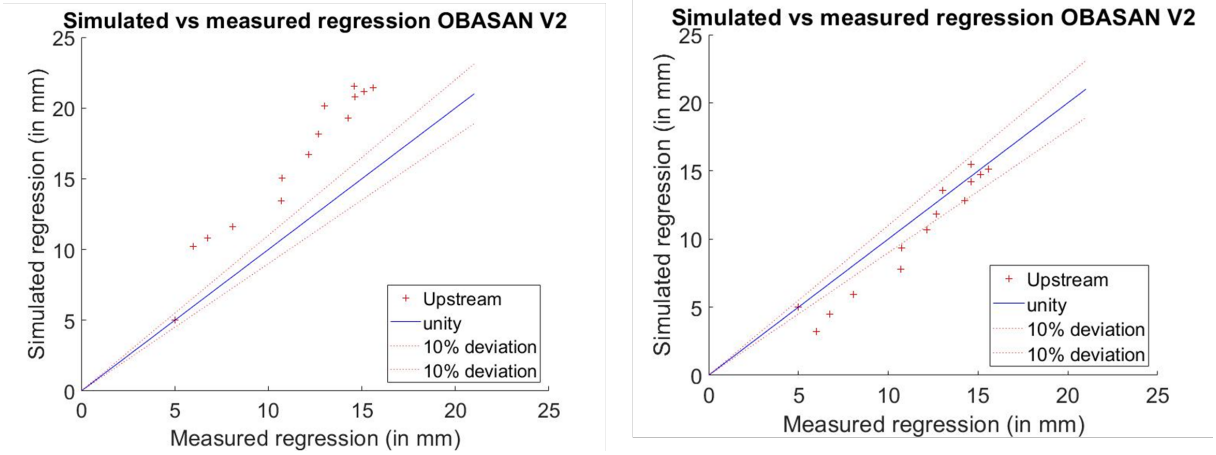

Figure 6.9: Ru O-BASAN02 measured vs simulated original (left) and corrected (right)

.

simulate the 40 kN class O-BASAN upstream regression.

6.2.2 Downstream fuel block measurement

The downstream end face averaged regression measurements for RIE and TTY data have already been calculated similarly to the correction method described above for the upstream end face. No further correction is therefore performed at this point.

6.2.3 Port measurement

The ports were measured by optically photographing the port from below (downstream side) as shown in Figure 6.10 and using this photograph to estimate the area of the port (green area), which is then approximated to a circle with the same area. This means that the downstream edge is used. This introduces an error as the actual regression of the port looks a bit more like shown in Figure 6.11 with the port diameter assumed to

be between the two red lines.

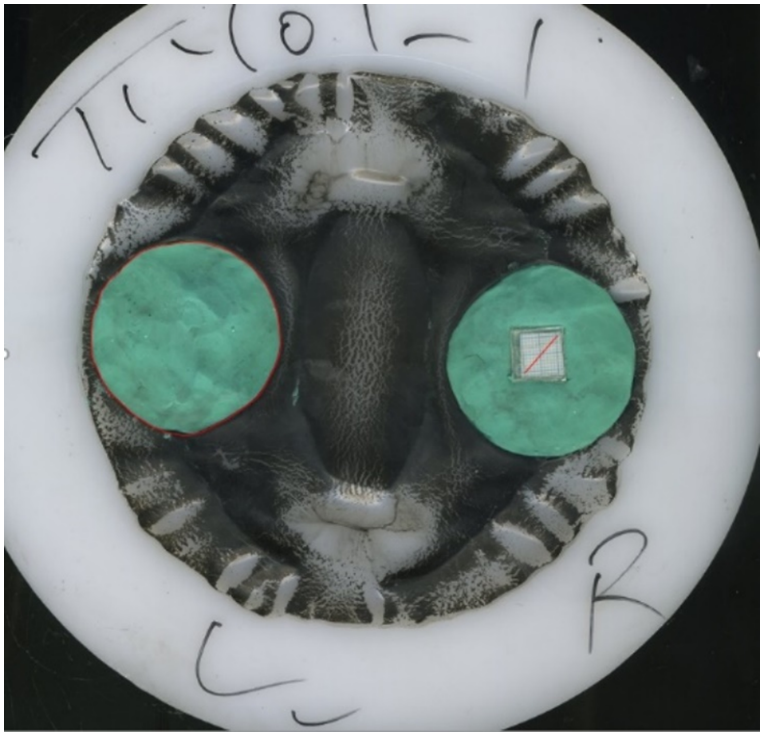

Figure 6.10: Port measurement method.

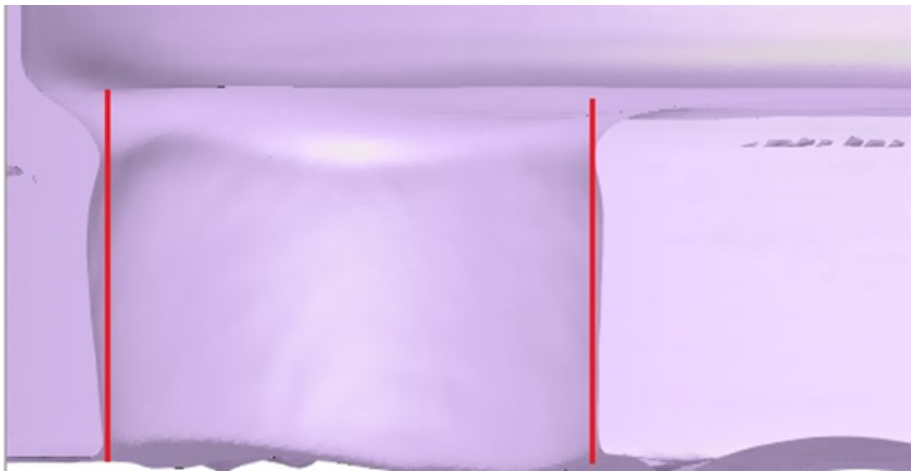

Figure 6.11: TTY 08 Block 01 port cross section of 3D scan.

As can be seen for the shown block (TTY 08 block 01), this is more representative of the minimum diameter and not the average diameter throughout the length of the port.

Apart from this single block, though (TTY 08 block 01), the 3D data, unfortunately, is not available and can not be recreated as the fuel blocks no longer exist. Therefore, though conceptually it is believed that the error is as described, this can not be verified and also can not be corrected from the existing data as was possible with the upstream end face. Overall, it is believed that the port regression is underestimated because of this measurement method.

6.2.4 Effect of scaling components in regression model

To follow up on the results from the scaling performance, it is interesting to have a look at the simulation of the regression with the scaling components removed, i.e., basing the simulation on Equations 2.8-2.10. Looking at the regression simulation of the O-BASAN engine done with RIE-based analysis, the side-by-side comparison with the simulation done with and without the scaling factors is shown in Figure 6.12 and Table 6.3.

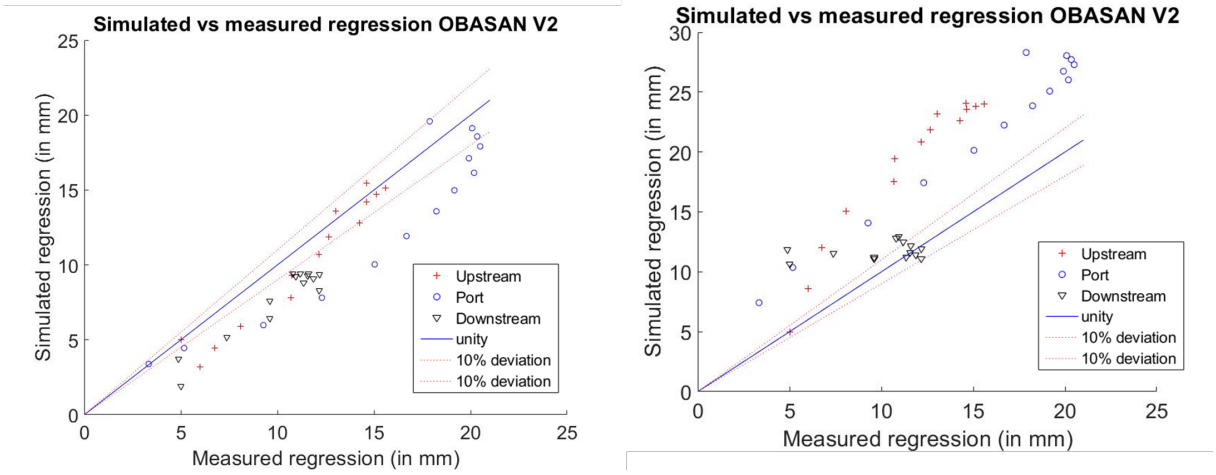

Figure 6.12: Simulator performance with (left) and without(right) scaling components

Table 6.3:: Simulated port regression error (RMS).

Simulation	With scaling	Without scaling
Upstream error rms (%)	22	49
Port error rms (%)	28	44
Downstream error rms (%)	24	49
Overall error rms (%)	25	44

Chapter 7

Discussion

The overarching goal of this research was to enable the development of a large-scale CAMUI type engine of a commercially viable launcher category size based on the extensive and rich data set of previous CAMUI research. To accomplish this, the first step was to build a comprehensive regression simulator based on the mathematical model developed over the last decade by the LSS laboratory. One of the targets of this new simulator was to take into account the scaling of the engine that happens during firing. This is linked to the question of the regression not being linear over time (16), (17) and, therefore, the unscaled conditions from start to end of a burn start being dubious with long burn time engines.

With the time stepped implementation developed in this research, this in principle should rectify to a large part this issue. However, this baseline implementation showed considerable deviations between simulated and measured results. An uncertainty analysis was performed to identify the simulator's most critical uncertainties and potential errors to improve the performance.

7.1 Uncertainty Analysis

As discussed in Chapter 4, the important uncertainties were found to be:

- LOX travel time/2 phase flow
- Local burn surface gasification
- *Re* number
- model assumptions for the first upstream end face
- burn time

Regarding the LOX travel time, the uncertainty caused by this travel time to the burn time was the potential most significant simulator error cause. Burn times and LOX flow rates are independently changed for each engine firing. This causes the large theoretical range in input errors seen in Table 4.4. In practicality, though, this uncertainty can be minimized as long as the LOX travel time is known or predictable and is considered in the simulator. To reduce this error in the first place, it is best to design the test setup with as short a flow distance between the pre-firing LOX (in tank or feedline) and the engine (injector) as possible.

For the local burn surface gasification, its effect on the O/F ratio causes the most significant potential simulation error. In contrast, the potential error caused by the change in mass flux is comparatively negligible. The additional fuel mass resulting from the local gasification is in the same order of magnitude for all the burn surfaces. At the same time, the O/F ratio varies by orders of magnitude from the first to the last burn

surface. Therefore, the input error differs considerably, as seen in Table 4.4, with the first burn surface seeing the most significant potential error and the last burn surface seeing the smallest potential error.

There is a considerable variation in Reynolds number between the individual engines and between the fuel blocks of a single engine. Furthermore, from (11) it seems that the m exponent does not follow the Reynolds number linearly. Together, these cause the large potential input error range for the m value seen in Table 4.4. As discussed in (8) though, once the Re number reaches a certain level, the m value levels out.

Overall, the first fuel block upstream end face stands out as having more significant simulation errors. It is believed that basing the regression model only on convective heat transfer effects is insufficient for this first burn surface, and that allowing for the effect of direct physical contact between the oxidizer and the fuel surface, causing a direct chemical reaction in the regression model, would be needed to model this surface correctly. Furthermore, the first upstream end face is also the most sensitive to errors in the O/F ratio, like the one caused by not including local fuel gasification.

7.2 Uncertainty corrections

To not have these effects on the regression simulation of the other blocks, an artificial correction has been implemented to always keep the first upstream end face regression rate correct compared to the measured results. It was seen that implementing this correction had a significant positive effect on reducing the errors seen on the downstream fuel blocks, supporting that the errors from the upstream regression rates propagate

downstream to negatively affect the regression modeling of the downstream burn surfaces.

It is important to note that implementing this artificial correction is helpful for large-scale development. A single firing will give this corrective factor for this first upstream end-face. Upon implementation, the whole engine design can confidently be designed based on the regression simulator. Note that traditionally, the last downstream end face has had relatively large modeling errors. These though have not been investigated in this work.

The tank pressurization time is taken into account in the simulator and, as such, is not a significant cause of uncertainties. The start-up transient it causes, though, is more problematic even if it is correctly measured as it is believed that a large start-up transient distorts the assumed regression rate value as described in Section 5.3.

Compared with a typical graph of the TTY series as shown in Figure 4.4, the transient times of the MSS engines have been considerably reduced from around 2 seconds to about 0.5 seconds showing that with a focus on the transient time in the test setup, these transient times can be significantly reduced. This was mainly through pre-pressurization of the LOX tank but also through the use of feedline pre-cooling. This was with the exception being the MSS06 which, as expected, had a transient of roughly 2 seconds as it was not pre-pressurized. This is despite pre-cooling of the feedline confirming that the primary critical transient effect comes from the LOX pressurization time.

When the scaled test setup does not allow for a short transient design, or when using heritage data with a long transient time, it is desirable to be able to correct the data to reflect the uncertainties caused by the long start-up transients.

A methodology for this was developed in the form of the burn time correction or the equivalent burn time. This equivalent burn time was developed, and its performance was evaluated.

7.2.1 Equivalent burn time

As is seen in Fig. 5.15 (left), the baseline performance of the regression simulator using nominal burn time shows good results for the RIE series port regression and results in an error RMS of 15% while using the equivalent burn time considerably increases the error to an RMS of 41%. Similar results are seen in Fig. 5.16 (left) with the error RMS increasing from 14% for nominal burn time to 24% for equivalent burn time. This follows the expectations as the best results for cases where the analysis and simulated engines are the same (with the analysis engines averaged) should be achieved with nominal burn time. The RIE series has a relatively larger difference between burn time and start-up transients than those of the TTY series. They have similar transient times, but the TTY series has considerably longer burn time. Because of this, the effects of the equivalent burn time are expected to be more significant for the RIE series, as was also seen in Fig. 5.15 and Fig. 5.16.

In contrast to this, when using the RIE-series in the constants analyzer and simulating the MSS-Lo port regression (Fig. 5.15 (right)), the use of equivalent burn time shows a substantial positive effect on the simulation accuracy. With the equivalent burn time implementation, the simulated regression error RMS is reduced from 41% with nominal burn time to 18 %. As the RIE-series analyzed have relatively short burn times and long start-up transients compared to the MSS-Lo, these results fit what is expected

from the equivalent burn time concept. With the equivalent burn time implementation, the simulator correctly predicts how the regression would be when RIE-series short burn time is extended in the long-burning MSS-Lo series. The shorter transient times of the MSS-Lo engines compared to the RIE engines further strengthen this. Similar results are seen in Fig. 5.16 (right) with the simulation of the MSS-Hi based on the TTY-series analysis. Here the error RMS is reduced from 27% to 24%. It is clear, though, that the effect is much smaller in this case. This is expected as the TTY and MSS-Hi engines have much more similar burn times than the RIE and MSS-Lo engines do.

When expanding the analysis to all burn surfaces, for the cases where the simulated and analyzed engines are the same, we again see the decrease in performance as expected. The use of equivalent burn time as shown in Figs. 5.17 (left) and 5.18 (left) does not clearly show an improvement over the use of nominal burn time. As mentioned in Chapter 4, several other uncertainties affect the regression simulator for the upstream and downstream surfaces. It is believed that what is seen here is that the overall regression modeling uncertainties for the fore- and back-end surfaces are too large to allow for a correct evaluation of the effect of the equivalent burn time on these surfaces. It is important to note that the implementation of equivalent burn time does not seem to considerably decrease the performance of the regression simulation of these burn surfaces.

The above discussion shows that errors in regression modeling caused by start-up transients can be improved under certain conditions by implementing the equivalent burn time. These conditions are, more specifically, when the simulated engine has a longer burn time and or shorter transient time than the engines used for the analysis.

To better define "longer" and "shorter" the effect on error RMS of each engine has been plotted in Fig. 7.1.

The data points have been interpolated for better visualization creating a 3D surface. The data points from each individual engine are shown (pink circle) with:

- Error reduction (delta error RMS) = error RMS (tb) – error RMS(tb_{eq})
- burnt time ratio = tb (simulated) / tb (analyzed)
- transient time ratio = tt (analyzed) / tt (simulated)

The times, tt (analyzed) and tb (analyzed), are the averaged times of all the engines in the analysis test series matching the given simulated engine. The simulated times are for each individual engine.

As simulated burn time increases and the simulated transient times decrease compared to the analyzed values, the error reduction increases when using the equivalent burn time. This is illustrated in Fig. 7.1. Looking at the same graph from a top view as shown in Fig. 7.2 a clear demarcation line (yellow) can be seen, which shows the border between when it is advantageous to use equivalent burnt time (above of the yellow 0-value line) and when it is disadvantageous (below the yellow line).

The author believes that, based on the above discussion, the use of equivalent burn time is valid with the given conditions, namely when simulated engines have longer burn time or shorter transient times, as shown in Figures 7.1 and 7.2. Within the overall performance of the current regression model, this can, for the end face surfaces, not yet be validated as other modeling uncertainties overshadow the effects of the equivalent burn time for end faces. The validation of the use for the port regression modeling also

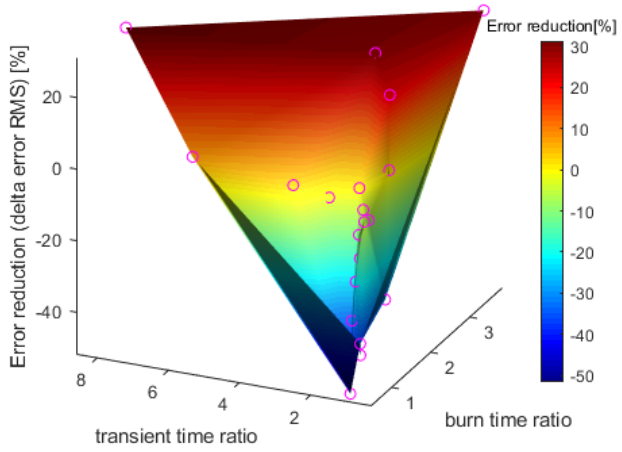

Figure 7.1: Equivalent burn time effect

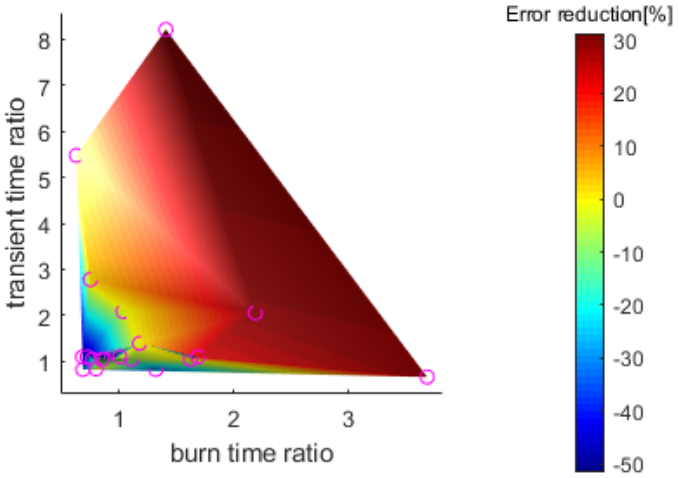

Figure 7.2: Equivalent burn time effect (top view)

shows that this method is valid for use on all conventional cylindrical hybrid rocket engines.

7.3 Scalability

With the implementation of the improvements investigated in Chapter 5, the regression model allowed MSW to design and safely fire the large-scale O-BASAN engine. The overall thrust simulation based on simulated regression rates shows a very similar thrust curve. The first thing to notice is that the peaks are opposite of the measured thrust. This is caused by the simulation being based on the LOX flow measurements of the test firing. A pressure peak in the chamber will show as a pressure peak in the downstream LOX orifice pressure, causing an apparent LOX flow reduction. The LOX travel time causes a time discrepancy between the simulated and measured thrust peaks. Furthermore, as pressure will propagate faster than the LOX flow will change, these pressure peaks are not representative of the actual LOX flow. Secondly, the simulated thrust drops compared to the measured thrust through the burn time. This is believed to be caused by the simulator using a fixed Isp value where in reality, the engines are designed to have optimal Isp at between 30% and 50% of the designed burn time. This means the optimal Isp for the O-BASAN is reached at between 7 and 10 seconds. This optimization of Isp counteracts the reduction in regression rates and, therefore, overall mass flux and is not implemented in the simulator. For the regression simulation, the first results from the O-BASAN engine showed excellent scalability of the model all the way from the RIE (2.5 kN) to the O-BASAN (40 kN). Though the O-BASAN engine was initially designed using the analysis of the TTY engines, using the regression model to simulate the O-BASAN based on the RIE only increased the RMS error from 22% (using TTY analysis) to 26% (RIE analysis). This supports the research done in (8) speculating that at high Reynolds numbers, the change in m value decreases and becomes

less important.

The results, though, do show errors both in the baseline and that the RMS error does increase with scaling. One of the errors believed to cause this was identified to be the different measurement methods used to measure the regression of the fuel blocks between the different engine series. Investigating this further, a systematic error in the measurement of the Upstream end face of the RIE and TTY engine series fuel blocks was identified.

As the fuel blocks are no longer available, this could not be directly corrected, but a mathematical correction was proposed based on the original measurement data. The first preliminary results, as shown in Figure 6.9 support this, though the further investigation into the effect of this correction on the overall simulator performance was not performed. Furthermore, based on the data from a single fuel block, it seems that the port regression measurement method, which was also different for the different engines, likewise had a different systematic error. However, this could not be further investigated apart from the single 3D scanned fuel block as not enough data was available to continue the investigation. These measurement errors are not seen when simulating the RIE or TTY themselves, as the measurement method used in the analysis and for the comparison are the same. For this reason, they also have only minimal if any impact on previous research.

The overall mass flux range of the researched engines are also borderline to what is usually considered nominal range for diffusion limited regression modelling (18). This is also believed to contribute to the seen error.

Lastly, to investigate the overall effect of the scaling law used, simulation of the

O-BASAN engine based on the RIE analysis was done with and without including the scaling terms of the regression model. As can be seen in Figure 6.12 and Table 6.3, the scaling components in the regression model considerably cut the simulation error of all 3 surfaces. Note that the Port regression measurements are still believed to be under measured. Correcting this would give a larger simulated port regression, further increasing the difference between using the scaling components or not.

Chapter 8

Conclusion

This research aimed to investigate the possibility of using the CAMUI regression model to predict the regression of large commercial-sized engines based on the regression data from smaller university-project-sized engine firings.

A CAMUI engine time stepped simulator was implemented for hybrid engine performance design purposes. Engine test fire data were compared with simulated results, and overall regression simulator errors of up to a factor of 2 were found.

The identified possible causes were discussed, and their potential effect on the regression simulator performance was presented. This led to identifying some key points that were then the focus of the further research presented here. Most important among these was implementing the burn time correction, which was developed to address the problem of start-up transients' effect on burn time definition and, therefore, regression simulation. Though inconclusive for the end face regression surfaces, for port regression, thus also for other types of cylindrical port hybrid rocket fuels, the equivalent burn time methodology was shown to be a valuable tool to reduce errors caused when short

burn time engines with relatively large start-up transients are used as a baseline to simulate the performance of longer burn time engines or shorter transient time engines. Equivalent burn time is, therefore, now an integral part of the overall CAMUI simulator and is being used for future engine designs.

With this and the other improvements, including implementing the localized fuel gasification, the final model showed good scalability over an extensive scaling range. In this case, up to a factor 16 in thrust class within an RMS error of 26%. This has allowed MSW to proceed with the ongoing development of a mass optimized commercial version of the 40 kN class engine based on the regression model but furthermore shows that, for CAMUI, small scale university engines can be used to correctly predict the regression and thereby the overall performance of much larger commercial-sized motors.

References

[1] O. Cecil and J. Majdalani, "Several hybrid rocket technologies hit advanced test stages," *Aerospace America*, vol. 11, p. 54, 2017.

[2] A. TAKAHASHI and T. SHIMADA, "Essentially non-explosive propulsion paving a way for fail-safe space transportation," *TRANSACTIONS OF THE JAPAN SOCIETY FOR AERONAUTICAL AND SPACE SCIENCES, AEROSPACE TECHNOLOGY JAPAN*, vol. 16, no. 1, pp. 1–8, 2018.

[3] L. Kamps, S. Hirai, and H. Nagata, "Hybrid rockets as post-boost stages and kick motors," *Aerospace*, vol. 8, no. 9, 2021.

[4] "Development of camui hybrid rocket to create a market for small rocket experiments , author=Nagata, H. and Ito, M. and Maeda, T. and Watanabe, M. and Uematsu, T., and Totani, T. and Kudo, I, journal=Acta Astronautica, volume=11, number=54, pages=253-258, year=2006, doi=10.2322/tastj.16.1,"

[5] H. Nagata, T. Ishiyama, Y. Inaba, R. Kanai, M. Wakita, T. Totani, and T. Uematsu, *Scale Effects on Combustion Characteristics of CAMUI-type Hybrid Rocket Motors*. 2015.

[6] G. Henry, R. Humble, W. Larson, N. Aeronautics, and S. Administration, *Space Propulsion Analysis and Design*. College custom series, McGraw-Hill, 1995.

[7] H. Nagata, H. Shunsuke, Y. Kaneko, M. Wakita, T. Totani, and T. Uematsu, *Development of Regression Formulas for CAMUI Type Hybrid Rockets as functions of Local O/F*, p. 7117. 2010.

[8] T. Ishiyama, "High reynolds number," Master's thesis, Hokkaido University, 2013.

[9] V. Tor and H. Nagata, "Error analysis for camui type hybrid rocket regression simulation," *TRANSACTIONS OF THE JAPAN SOCIETY FOR AERONAUTICAL AND SPACE SCIENCES, AEROSPACE TECHNOLOGY JAPAN*, vol. 17, no. 4, pp. 519–524, 2019.

[10] H. Nagata, "Development of a liquid oxygen supply system for a small-scale sounding rocket," *Japanese Journal of Multiphase Flow*, no. 27, pp. 393–400, 2013.

[11] H. Nagata, M. Nohara, R. Kanai, M. Wakita, and T. Totani, "Effects of reynolds number and flow channel geometry on fuel regression characteristics in camui type hybrid rocket," in *36th IAC, Naples, Italy*, 2006.

[12] T. Viscor, H. Isochi, N. Adachi, and H. Nagata, "Burn time correction of start-up transients for camui type hybrid rocket engine," *Aerospace*, vol. 8, no. 12, 2021.

[13] R. A. Frederick and B. E. Greiner, "Laboratory-scale hybrid rocket motor uncertainty analysis," *Journal of Propulsion and Power*, vol. 12, no. 3, pp. 605–611, 1996.

[14] G. Cai, C. Li, S. Zhao, and H. Tian, "Transient analysis on ignition process of catalytic hybrid rocket motor," *Aerospace Science and Technology*, vol. 67, pp. 366–377, 2017.

[15] T. Viscor, L. Kamps, K. Yonekura, H. Isochi, and H. Nagata, "Large-scale camui type hybrid rocket motor scaling, modeling, and test results," *Aerospace*, vol. 9, no. 1, 2022.

[16] R. Kumar and P. A. Ramakrishna, "Issues related to the measurement of regression rate of fast-burning hybrid fuels," *Journal of Propulsion and Power*, vol. 29, no. 5, pp. 1114–1121, 2013.

[17] D. Bianchi, F. Nasuti, and C. Carmicino, "Hybrid rockets with axial injector: Port diameter effect on fuel regression rate," *Journal of Propulsion and Power*, vol. 32, no. 4, pp. 984–996, 2016.

[18] M. Chiaverini and K. Kuo, *Fundamentals of Hybrid Rocket Combustion and Propulsion*. Progress in astronautics and aeronautics, American Institute of Aeronautics and Astronautics, 2007.